EEET ECOLOGICAL ENGINEERING & ENVIRONMENTAL TECHNOLOGY

Ecological Engineering & Environmental Technology, 2026, 27(6), 426–450
https://doi.org/10.12912/27197050/221824
ISSN 2719–7050, License CC-BY 4.0

Received: 2026.04.17
Accepted: 2026.05.18
Published: 2026.06.01

Quantifying aboveground carbon at risk and composite vulnerability in semi-arid mountain forests: A Landsat and field-inventory approach in the Moroccan High Atlas

Ayoub Sguigaa[1*], Said Lahssini[1], Said Moukrim[2], Imane Sebari[3], Kamal Menzou[1], Hassan Rahoui[1], Abdellatif Khattabi[1], Ali Azedou[1]

[1] National School of Forestry Engineers, Salé, Morocco
[2] Mohammed V University of Rabat, Rabat, Morocco
[3] Agronomic and Veterinary Institute Hassan II, Rabat, Morocco
* Corresponding author's email: ayoubsguigaa@gmail.com

ABSTRACT

This study aims to quantify aboveground carbon at risk in semi-arid mountain forests of the Moroccan High Atlas and to test whether composite vulnerability is higher in structurally dense stands than in open stands. A 30-year Landsat time series (1995–2025) was analysed using LandTrendr applied to the normalized burn ratio (NBR) index, combined with probabilistic field inventory data and penalized logistic regression. A composite vulnerability index was developed by integrating disturbance probability, spectral severity, and recovery capacity, with climatic predictors including precipitation seasonality, heat load index, and 12-month SPEI. Total aboveground carbon stock was estimated at 122,474 tC, of which 15,985 tC (13.05%; 95% bootstrap CI: 11,654–20,293) is classified as at risk. A pronounced hotspot in dense forest strata accounts for 40.4% of carbon at risk while covering 26.2% of the area. After accounting for collinearity with elevation, precipitation seasonality emerged as the only significant predictor of disturbance probability ($\beta = 1.184$; $p = 0.002$; AUC = 0.827), providing partial support for the hypothesised climatic control on disturbance. Field validation against mortality observations showed perfect sensitivity (1.000) and moderate specificity (0.478), indicating a tendency toward early detection of partial dieback rather than omission of true events. The results suggest that structurally dense stands concentrate a disproportionate share of carbon vulnerability, consistent with a climatic maladaptation mechanism linked to past establishment conditions under more favourable moisture regimes. However, estimates should be interpreted as conservative upper bounds due to moderate model specificity (0.478), uncertainty in spectral proxies for disturbance and recovery, and limitations in stratum-level biomass generalisation. The framework provides a reproducible approach for mapping carbon at risk by integrating remote sensing, field inventories, and climate data, and can support prioritisation of monitoring and management interventions such as targeted thinning and regeneration assistance in high-risk dense stands. The main contribution lies in delivering a transferable methodology for quantifying spatial carbon vulnerability in semi-arid forest ecosystems where empirical data remain scarce.

Keywords: carbon at risk, composite vulnerability, climate resilience, forest disturbance, drought, Mediterranean forests, High Atlas, LandTrendr.

INTRODUCTION

The Mediterranean Basin has experienced sustained warming and aridification since the mid-twentieth century, and climate projections agree on a future increase in the frequency and severity of droughts (IPCC, 2022; Tramblay et al., 2020). This trend translates into reduced soil moisture, captured by indices that integrate potential evapotranspiration, most notably the SPEI (Vicente-Serrano et al., 2010; Beguería et al., 2014). Drought-induced forest mortality has been documented on every continent, with cascading effects on ecosystem function (Allen et

al., 2015; Carnicer et al., 2011; Camarero et al., 2015). At regional scales, these dynamics can locally weaken or reverse the carbon sink, eroding the mitigation potential of climate policies (Anderegg et al., 2020; Pan et al., 2011). The southern rim of the basin combines pronounced projected drying with a persistent observational gap (Forzieri et al., 2022; Senf and Seidl, 2021), which motivates the attention given here to Maghreb forests.

Advances in satellite remote sensing now allow the history of forest disturbances to be reconstructed at fine temporal and spatial scales. Landsat time-series segmentation algorithms, notably LandTrendr (Kennedy et al., 2010, 2018) and CCDC (Zhu and Woodcock, 2014), detect spectral breakpoints associated with dieback events and quantify their severity over several decades (Wulder et al., 2019). In parallel, spatially balanced probabilistic forest inventories yield unbiased ground-based estimates, whereas convenience plots tend to overrepresent accessible or productive stands (Cochran, 1977; Stevens and Olsen, 2004). The two approaches are complementary: remote sensing delivers exhaustive spatial coverage, while probabilistic inventories ensure inferential rigor. Their joint application remains underexploited in the Mediterranean forests of the Maghreb.

The framework of composite vulnerability proposed by Forzieri et al. (2022) combines three dimensions of forest response to disturbance: the probability that an event occurs, its spectral severity, and the subsequent recovery capacity (Allen et al., 2015). Compared with univariate indicators such as raw mortality, defoliation, or canopy loss, this framework ranks stands according to their joint exposure across the three dimensions, providing a basis for reproducible management prioritization.

The forests of the Moroccan High Atlas occupy a transition zone between Atlantic and Saharan influences, along an altitudinal gradient from 1.300 to 2.800 m that controls water balances. Holm oak (*Quercus rotundifolia*) dominates these stands at the southern margin of its range, where populations face higher climatic variability than those located in the core of the species distribution (Hannah et al., 2014). A history of forest management, including protection and assisted regeneration phases, has promoted the densification of certain stands under a water regime more favorable than today. This context provides an empirical setting for examining climatic maladaptation, namely the mismatch between establishment conditions and current conditions. Three gaps motivate the present work. First, no spatially explicit map of carbon at risk has yet been produced for a Moroccan forest province using a fully reproducible workflow combining probabilistic field inventories with long-term Landsat disturbance detection. Existing estimates rely either on convenience sampling or coarse-resolution global products that obscure within-province heterogeneity relevant for management. Second, early-warning indicators of forest vulnerability derived from spectral time series are rarely evaluated against independent field-based mortality data, limiting the ability to distinguish true ecological signals from artefacts of segmentation algorithms (Cailleret et al., 2017; DeSoto et al., 2020). Third, direct validation of remotely sensed disturbance and recovery metrics against systematic forest inventories remains scarce in Mediterranean North Africa, where most studies rely on indirect proxies such as canopy loss or defoliation rather than tree-level mortality observations (Cohen et al., 2018; Frazier et al., 2018).

To address these gaps, this study develops a fully reproducible framework that integrates probabilistic field inventory data, Landsat time-series segmentation, and climatic covariates to quantify and map aboveground carbon at risk in the forests of the Moroccan High Atlas (Azilal Province) over the period 1995–2025. The approach produces spatially explicit estimates of disturbance probability, severity, and recovery, combined into a composite vulnerability index and translated into carbon-at-risk metrics at the stratum scale.

We test two hypotheses. H1: precipitation seasonality and the minimum 12-month SPEI significantly explain the probability of spectral disturbance at the plot level, with an expected positive effect of precipitation seasonality (higher seasonality → higher disturbance probability) and an expected negative effect of the minimum 12-month SPEI (lower SPEI, i.e. more severe drought → higher disturbance probability), in line with the documented role of climatic water stress in Mediterranean forest stability (Vicente-Serrano et al., 2010; Beguería et al., 2014). H2: composite vulnerability (V_i) increases along the canopy-density gradient open → moderate → dense, such that the mean V_i of dense strata exceeds that of open strata.

MATERIALS AND METHODS

Study area

The study area extends over 26,123 ha of mountain forests in Azilal Province, Moroccan central High Atlas (Béni Mellal-Khénifra region; 31°37′–32°06′ N; 6°45′–6°20′ W; elevation 1.200–2.800 m; Figure 1). The climate is semi-arid Mediterranean with a montane regime. Annual precipitation ranges from 350 to 550 mm, falls mainly between October and March, and gives way to a dry season from May to September; mean annual temperature varies between 8 and 16 °C with elevation. Holm oak *Quercus rotundifolia* Lam. (syn. *Q. ilex* subsp. ballota) dominates the canopy and associates, depending on elevation and aspect, with *Juniperus phoenicea* L., *J. oxycedrus* L., *Pinus halepensis* Mill., *Tetraclinis articulata* (Vahl) Mast., *Cupressus arizonica* Greene (plantations), and *P. pinaster* Aiton (Ezzahiri and Belghazi, 2000). Recurrent droughts, grazing pressure, and wood harvesting have eroded the canopy since the late 1990s.

Sampling design and stratification

The forest mask was derived from a supervised Random Forest classification on Sentinel-2 Level-2A imagery (May–September 2025). The

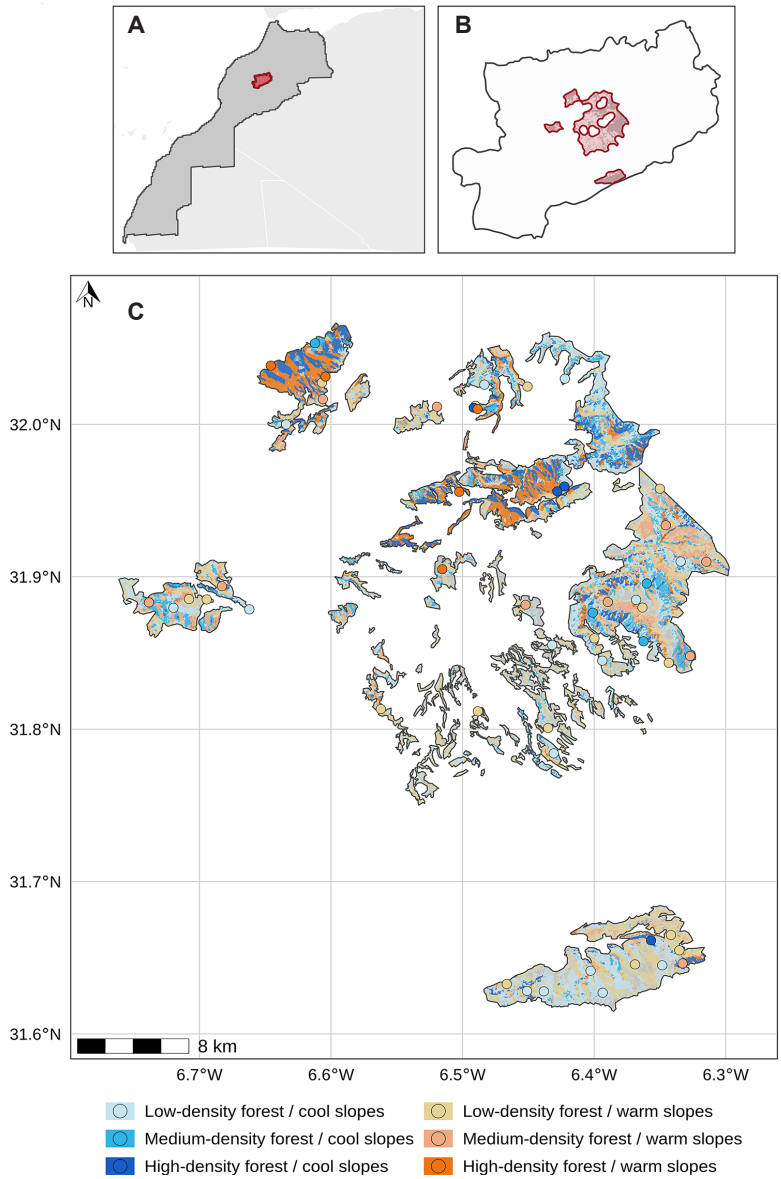

Figure 1. Study area in the central High Atlas, Azilal Province, Morocco: (A) location within Morocco; (B) forest units within the province; (C) stratification and location of the 60 GRTS plots across the study massif

Table 1. Stratification of the study area: six strata (26,123 ha total) crossing canopy density (Sentinel-2 Random Forest) with the heat load index (median threshold 0.74). Plot numbers (n) follow Neyman's rule

Stratum	Canopy density	HLI (aspect)	Area (ha)	% area	n
S1	Open (< 30%)	Cool (HLI < 0.74)	5.699	21.8%	18
S2	Open (< 30%)	Warm (HLI ≥ 0.74)	6.070	23.2%	17
S3	Moderate (30–60%)	Cool	3.848	14.7%	4
S4	Moderate (30–60%)	Warm	3.667	14.0%	11
S5	Dense (> 60%)	Cool	3.382	12.9%	5
S6	Dense (> 60%)	Warm	3.457	13.2%	5
Total	—	—	26.123	100.0%	60

resulting canopy density map of the study area is shown in Supplementary Figure S1. The ranking of the six predictors by Gini-impurity variable importance is shown in Supplementary Figure S2. Stratification crossed two orthogonal factors: canopy cover density, partitioned into Open (< 30%), Moderate (30–60%), and Dense (> 60%); and the Heat Load Index (HLI; McCune and Keon, 2002), computed from SRTM 30 m and dichotomized at its midpoint (threshold 0.74) into Cool and Warm classes. The spatial distribution of HLI over the forest mask is shown in Supplementary Figure S3. The crossing yielded six strata: S1 (Open-cool), S2 (Open-warm), S3 (Moderate-cool), S4 (Moderate-warm), S5 (Dense-cool), and S6 (Dense-warm) (Table 1). The corresponding spatial mosaic of the six strata is mapped in Supplementary Figure S4. A total of n = 60 plots were distributed across these strata using Neyman's optimal allocation (Cochran, 1977), which assigns sampling effort to each stratum in proportion to the product of its area and its within-stratum biomass variability:

$$n_h = n \times (A_h \cdot S_h) / \Sigma_k (A_k \cdot S_k) \quad (1)$$

where: n_h is the number of plots allocated to stratum h, n is the total sample size, A_h is the area of stratum h (ha), and S_h is the within-stratum standard deviation of aboveground biomass (Mg ha^{-1}).

Operational parameters and validation metrics of the stratification protocol, Random Forest classification accuracy, training sample composition, HLI dichotomization threshold are reported in Supplementary Table S3.

In the absence of a prior field inventory for the study area, S_h was estimated a priori from GEDI L4A footprints (Dubayah et al., 2020; Duncanson et al., 2022) used as a pre-inventory proxy, an approach recommended when no historical field data are available (Cochran, 1977; Chirici et al., 2012). The resulting allocation placed 35 plots in the open strata (S1 and S2), 11 in the moderate-warm stratum (S4), and 14 in the remaining moderate-cool and dense strata combined (S3, S5, S6); a floor of at least 4 plots per stratum was set to permit within-stratum variance estimation. Plot coordinates were generated by GRTS sampling (R package by Dumelle et al., 2023), which delivers equiprobable spatial coverage across the study area.

Forest inventory and estimation of aboveground biomass

Each circular plot covered 0.1018 ha with an 18 m radius. All trees with DBH ≥ 6 cm were inventoried, and the following variables recorded for each stem: species, DBH (cm, at 1.30 m), total height H (m), health status (live, lightly declining, severely declining, standing dead), and mortality signs over ≥ 15% of the trunk circumference. Per-tree aboveground biomass (AGB) was estimated through the three-factor chain prescribed by the IPCC Tier 2/3 guidelines (IPCC, 2019):

$$AGB = V \times \rho \times BEF \quad (2)$$

where: AGB is the per-tree aboveground biomass (kg), V the merchantable stem volume (m^3), ρ the basic wood density (t·m^{-3}), and BEF the dimensionless biomass expansion factor.

This factorisation is the standard route for Mediterranean forests (Montero et al., 2005; Ruiz-Peinado et al., 2011, 2012). It anchors the estimate in locally calibrated volume tables and avoids transposing allometries developed under

foreign biogeographic conditions (Henry et al., 2011; Chave et al., 2014).

The health-status classes below relied on field-based semi-quantitative visual estimation of crown and trunk symptoms; the percentage cutoffs given are operational reference values rather than measured fractions. The four health status classes were assigned in the field according to operational visual criteria. A tree was classified as live when its crown was predominantly green and functional, without marked drying, defoliation, or branch mortality. Lightly declining applied to trees still alive with moderate symptoms (partially dry foliage, limited defoliation, small dead branches) affecting less than approximately 30% of the crown. Severely declining was retained when declining symptoms (dead branches, marked defoliation, strongly reduced crown) dominated more than approximately 50% of the crown while a living portion remained visible. Field photographic examples of the four health classes are shown in Supplementary Figure S5. Standing dead applied to upright or rooted trees with no green foliage and no visible vegetative activity, confirmed by complementary signs such as detached bark, exposed dead wood, or dry brittle trunk. Mortality signs on the trunk, recorded when affecting approximately 15% or more of the circumference, denoted local cambium alteration or advanced degradation (detached or missing bark, exposed dead wood, necrotic patches, deep cracks, insect galleries, fungal fructifications, abnormal exudations, severe wounds from topping or pruning).

Standing timber volume was estimated using volume tables provided by Morocco's National Agency for Water and Forests (ANEF). Five volume tables apply to the dominant or co-dominant species of the study area: *Quercus rotundifolia, Pinus halepensis, Pinus pinaster, Tetraclinis articulata,* and *Cupressus arizonica*. The predictors used were stem girth at breast height, C (cm, measured at 1.30 m), and total tree height, H (m). Calibration sample sizes ranged from 35 to 100 trees per species, with coefficients of determination R^2 ranging from 0.911 to 0.985 and a mean relative bias below 5% (Table 2). Detailed validation statistics and operational diameter ranges are reported in Supplementary Table S1. Volumes were converted into biomass using species-specific basic wood densities, ρ, and then expanded to total aboveground biomass, AGB, using species-specific biomass expansion factors, BEFs (Table 2). The ρ values were taken from Vignote et al. (2006) for Q. rotundifolia, Montero et al. (2005) for the pines, El-Mouridi et al. (2011) for *T. articulata*, and Bárcenas-Pazos et al. (2008) for *C. arizonica*. BEF values were obtained from Ruiz-Peinado et al. (2011, 2012), Vallet et al. (2006), Shaiek et al. (2011), and Sghaier et al. (2015). No local volume tables were available for *Juniperus thurifera*, *J. phoenicea*, and *J. oxycedrus*. For these species, the direct AGB allometry developed by Montero et al. (2005) for *J. thurifera* in Iberian Mediterranean

Table 2. Volume tables and volume-to-aboveground-biomass conversion parameters by species. The V × ρ × BEF chain (Equation 2) is applied stem by stem for species with a local volume table; other species use an allometric equation predicting aboveground biomass directly, with BEF embedded

Species	V equation (dm^3)	R^2	N	DBH range (cm)	ρ ($t \cdot m^{-3}$)	BEF
Quercus rotundifolia	$V = -77.469 + 2.918 \cdot C + 0.002 \cdot C^2$	0.981	87	7–60	0.90	*1.40*
Pinus halepensis	$V = -122.033 + 5.217 \cdot C - 0.253 \cdot H \cdot C + 0.002 \cdot H \cdot C^2$	0.950	56	8–55	0.53	*1.42*
Pinus pinaster	$V = 0.075 + 0.097 \cdot H \cdot C + 0.038 \cdot H \cdot C^2$	0.985	35	8–36	0.51	*1.32*
Tetraclinis articulata	$V = -10.263 + 0.465 \cdot C + 0.013 \cdot C^2$	0.911	86	7–23	0.59	*1.45*
Cupressus arizonica	$V = 21.103 + 0.003 \cdot H \cdot C^2$	0.983	100	6–29	0.48	*1.35*
Juniperus thurifera	$Ws = 0.0132 \cdot D^2 \cdot H + 0.217 \cdot D \cdot H$	—	—	—	0.55	*embedded*
Juniperus phoenicea	Proxy: J. thurifera	—	—	—	0.55	*embedded*
Juniperus oxycedrus	Proxy: J. thurifera	—	—	—	0.55	*embedded*

Note: V = standing timber volume (dm^3); C = circumference at 1.30 m (cm); H = total tree height (m); D = diameter at 1.30 m (cm), with $D = C/\pi$; ρ = basic wood density (oven-dry mass / saturated volume); BEF = biomass expansion factor (= total AGB / standing-timber AGB); Ws = aboveground stem biomass (kg). For species without a local volume table, the equation predicts aboveground biomass directly and the BEF is embedded in the model (labeled "embedded"). R^2, N, and DBH range correspond to the calibration of each yield table and apply only to species with a local volume table.

stands was used, with BEF embedded in the equation. The same equation was applied as a proxy to *J. phoenicea* and *J. oxycedrus*, all three species sharing membership in the Mediterranean Cupressaceae and similar basic wood densities ($\rho \approx 0.55$ $t \cdot m^{-3}$). The implications of this substitution are discussed in the Limitations section.

The sensitivity of total AGB to the choice of ρ and BEF was assessed through a Monte Carlo simulation. For each species, ρ and BEF were independently multiplied by random factors drawn from normal distributions N(1, σ_ρ²) and N(1, σ_BEF²), with σ_ρ = 0.10 and σ_BEF = 0.15. These standard deviations bracket the dispersion observed across published BEF values for Mediterranean species (Montero et al., 2005; Ruiz-Peinado et al., 2011, 2012) and the inter-source variability documented in our reference set. Ten thousand iterations were drawn (R base random number generator, seed 2024), producing empirical distributions for total AGB, total carbon stock and species-level subtotals. The full Monte Carlo distribution of total AGB is shown in Supplementary Figure S10. The 90% confidence interval [p5; p95] is reported as a measure of methodological uncertainty associated with the conversion parameters. Across the 60 inventoried plots, the *Juniperus* genus accounted for 3.65% of the total aboveground biomass of the study area; the proxy substitution applied to *J. phoenicea* and *J. oxycedrus* therefore concerned 3.61% of the total AGB. Per-tree aboveground carbon is obtained as:

$$C_{tree} = AGB \times CF \quad (3)$$

where: C_tree is the per-tree aboveground carbon (kg), AGB the per-tree aboveground biomass from Equation 2, and CF the dimensionless biomass-to-carbon conversion factor.

The default IPCC value CF = 0.47 (IPCC, 2019) for non-tropical forests was adopted, which keeps the estimates comparable with the Moroccan national inventories and with FAO reporting.

The aboveground biomass density per stratum is obtained by summation over the stratum:

$$AGBD_{stratum} = (\Sigma_i AGB_i \times 10^{-3}) / (n_{plots} \times 0.1018) \quad (4)$$

where: $AGBD_{stratum}$ is the aboveground biomass density of the stratum (Mg ha^{-1}), AGB_i is the aboveground biomass of tree *i* (kg), *n_plots* is the number of plots inventoried in the stratum, and 0.1018 is the area of a single plot (ha).

Landsat temporal segmentation with LandTrendr

Landsat Collection 2 Level-2 Surface Reflectance imagery (30 m, 1995–2025; Landsat 5/7/8/9) was retrieved through Google Earth Engine (Gorelick et al., 2017). Cloud and shadow masking relied on the embedded QA_PIXEL band, and inter-sensor radiometric harmonization followed Chastain et al. (2019). A C-correction topographic normalization was applied prior to index computation to mitigate illumination bias in the mountainous terrain of the High Atlas. Annual composites were built as pixel-wise medians over the growing season May–September (Julian days 121–273), the phenologically most stable period for the dominant species. Data availability was tracked through the count of valid observations per pixel and per year (NOBS); years with mean NOBS below six were flagged as low quality, mostly during the Landsat-7 SLC-off period (2003–2012) (Figure 2).

LandTrendr (Kennedy et al., 2010, 2018) was run in Google Earth Engine (Gorelick et al., 2017) on the Landsat Collection 2 Surface Reflectance archive (TM, ETM+, OLI) for the 1995–2025 window. The normalized burn ratio (NBR) was retained as the primary spectral index, on account of its known sensitivity to canopy loss in Mediterranean sclerophyllous vegetation (Cohen et al., 2018; Frazier et al., 2018). Annual radiometric quality was tracked through the count of valid observations per pixel, with the Landsat-7 SLC-off window (2003–2013) treated as a known weak point. The full set of LandTrendr parameters, optimised for the detection of gradual disturbances typical of semi-arid Mediterranean forests, is reported in Table 3.

LandTrendr returned, for each pixel, the year of the main disturbance (year of disturbance), its magnitude (×1000 in index units), its duration (years), and the magnitude of the subsequent recovery segment. Plot-level metrics were aggregated within a 45 m circular buffer (3 × 3 Landsat pixel window, nine 30 m pixels). This buffer mitigates geolocation errors (orthorectification accuracy ±15 m; Wulder et al., 2019) and dampens pixel-to-pixel noise in the annual composites. A binary disturbance status (disturb_bin) was assigned at plot level: disturb_bin = 1 when more than half of the pixels in the 3 × 3 neighborhood (≥ 5 of 9) underwent a LandTrendr loss segment between 1995 and 2025, and disturb_bin = 0 otherwise. Disturbances

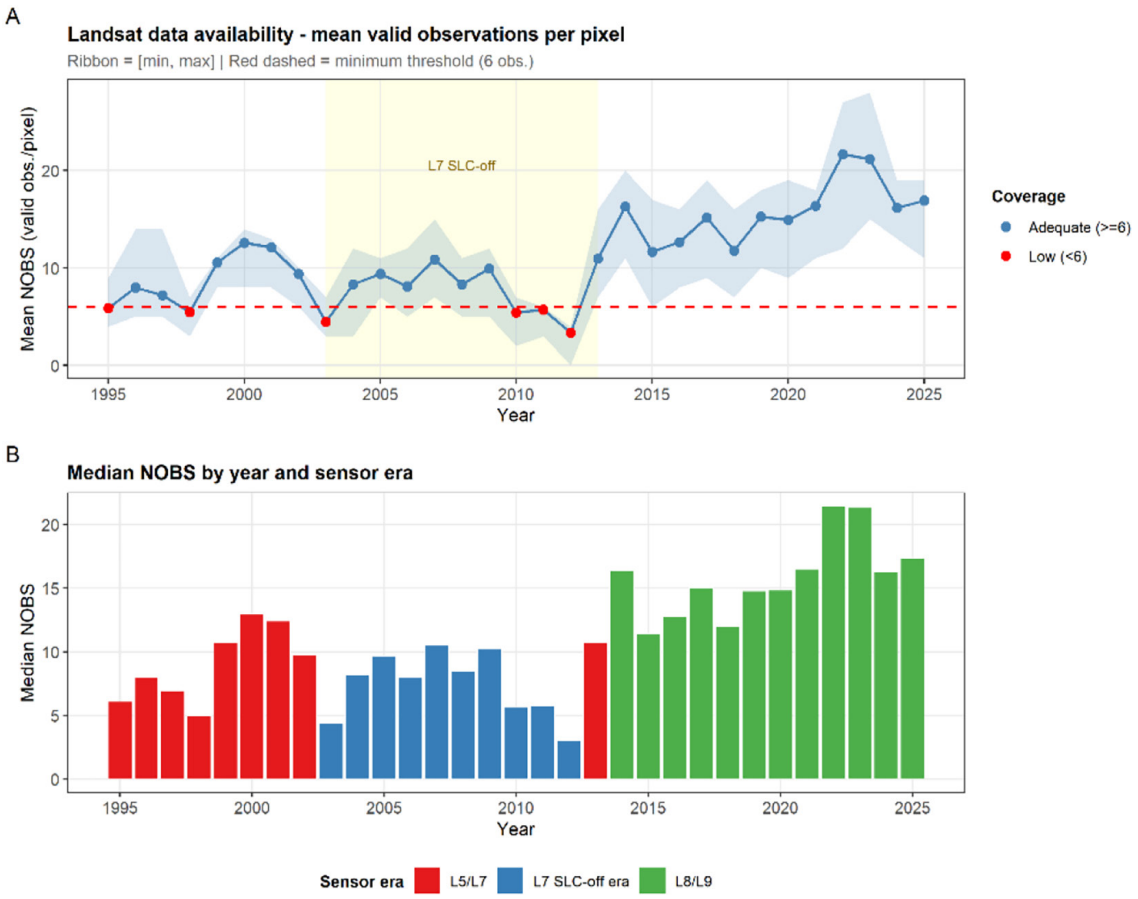

Figure 2. Annual availability of valid Landsat observations per pixel (NOBS) over the study area, 1995–2025. (A) Mean NOBS per year (blue line), with ribbon showing the [min, max] range across pixels and red dashed line marking the minimum threshold (6 observations). Years with mean NOBS < 6 are highlighted in red. The Landsat-7 SLC-off period (2003–2012) is shaded in yellow. (B) Median NOBS by year and sensor era: L5/L7 (red, 1995–2002), L7 SLC-off (blue, 2003–2012), L8/L9 (green, 2013–2025)

Table 3. LandTrendr parameters for the 1995–2025 Landsat time series, optimised to detect gradual disturbances typical of semi-arid Mediterranean forests

Parameter	Value	Justification
Primary spectral index	NBR	Optimal sensitivity to canopy loss (Cohen et al., 2018)
Max segments	6	Captures multi-temporal dynamics (Kennedy et al., 2018; Pasquarella et al., 2022)
Spike threshold	0.9	Filters annual radiometric noise while preserving the multi-year signal
Vertex count overshoot	3	Default pruning tolerance (Kennedy et al., 2018)
Prevent one year recovery	true	Prevents spurious one-year spectral rebounds, inconsistent with the slow regeneration dynamics of semi-arid xeric forests
Recovery threshold	0.25	Enforces recovery over at least four years, consistent with the slow regeneration dynamics typical of xeric sclerophyllous forests
Pval threshold	0.10	Internal threshold of the Levenberg–Marquardt optimization, adapted to short, noisy Landsat series (SLC-off window 2003–2013) typical of semi-arid Mediterranean studies (Pasquarella et al., 2022). This threshold is not a criterion of ecological significance at the pixel level.
Best model proportion	0.75	Default trade-off between goodness of fit and model parsimony
Min observations needed	6	Minimum usable series length, adapted to the Landsat-7 SLC-off period (Kennedy et al., 2010)
Annual composite	May–September median	Period of phenological stability
Spatial resolution	30 m	Landsat Collection 2 Surface Reflectance

were further partitioned by segment duration into three strictly disjoint classes: abrupt (duration ≤ 1 year), gradual (1 < duration ≤ 4 years), and chronic (duration > 4 years).

Statistical analyses

Four explanatory variables were retained at plot level. Two captured topographic and bioclimatic exposure: the heat load index (HLI) and elevation, both derived from the SRTM 30 m digital elevation model (McCune and Keon, 2002). Two captured climatic forcing: precipitation seasonality (WC_Pseas_CV, WorldClim BIO15) (Fick and Hijmans, 2017) and the annual minimum 12-month SPEI (Vicente-Serrano et al., 2010; Beguería et al., 2014), this last variable computed over 1995–2025 from CHIRPS precipitation (Funk et al., 2015) and ERA5-Land reanalysis (Muñoz-Sabater et al., 2021). All variables were centered and scaled before analysis, so that coefficients could be compared on a common scale; collinearity was then diagnosed by Pearson correlation and variance inflation factors (VIF).

Extraction procedure for plot-level pre-disturbance climatic variables

For plots flagged as disturbed by LandTrendr (disturb_bin = 1), retrospective 3- and 12-month windows preceding the main year of disturbance were extracted from two monthly datasets: CHIRPS for precipitation (Funk et al., 2015), and ERA5-Land for temperature, reference evapotranspiration (ETo), and vapor pressure deficit (VPD; Muñoz-Sabater et al., 2021). From these windows, four climatic descriptors were derived: the minimum 12-month SPEI preceding disturbance, the mean 12-month VPD, the cumulative water deficit (P − ETo) over 12 months, and the mean VPD over the shorter 3-month window. Plots whose pre-disturbance window fell at the very start of the LandTrendr time series were excluded for incomplete coverage. The relationship between magnitude (ΔNBR × 1.000) and each descriptor was then probed by simple linear regression.

Penalized logistic regression

The spectral probability $\hat{P}$ was estimated by Firth's penalized logistic regression (Firth, 1993; Heinze and Schemper, 2002; R package logistf), a method that controls bias for small samples and for quasi-complete separation. The response variable was disturb_bin (1 = disturbance detected, 0 = none). Three candidate models were compared. The reference model V2 used standard maximum likelihood with elevation, HLI, and minimum SPEI-12 as predictors. Model V5 fitted the same predictors under Firth's penalisation. Model V6-B substituted precipitation seasonality (WC_Pseas_CV) for elevation while keeping HLI and minimum SPEI-12, again under Firth's penalisation. This substitution was motivated by the strong near-collinearity between elevation and precipitation seasonality (Pearson r = −0.958; 95% CI [−0.976, −0.927]; p < 0.001; n = 52), which yielded a joint VIF of 12.1 for both variables in the four-predictor diagnostic block and therefore exceeded the joint-exclusion threshold (VIF > 10; Supplementary Figure S11). Precipitation seasonality was retained as the climatically interpretable surrogate of elevation, since it directly captures the Mediterranean rainfall regime that elevation conveys only indirectly in the High Atlas context. Within V5 (Elev + HLI + SPEI-12) and V6-B (Pseas_CV + HLI + SPEI-12) taken separately, all VIFs remained below 1.2, confirming the absence of residual collinearity once the two variables were not retained jointly. Model selection unfolded in three sequential steps. Collinearity was first diagnosed by variance inflation factors (VIF), with a joint-exclusion threshold of 10 (Hair et al., 2014). Predictive performance was then compared by leave-one-out cross-validation on the AUC. Finally, the robustness of the retained model was checked against Riley's conservative shrinkage threshold of 0.90 (Riley et al., 2019; van Smeden et al., 2019).

Normalized severity $\hat{S}$ was modelled by beta regression (Ferrari and Cribari-Neto, 2004), a regression family suited to responses bounded in the open interval (0, 1). The model was fitted on the subset of disturbed plots (disturb_bin = 1). The response was the relative magnitude MAG_rel = MAG / max(MAG_stratum), and the predictors were those of model V6-B. Spectral recovery $\hat{R}$ was computed plot by plot from the LandTrendr post-disturbance recovery segment and expressed on a [0, 1] scale across the full plot dataset. Undisturbed plots received $\hat{R} = 0$ by convention. The composite spectral vulnerability index V_i was then assembled as:

$$V_i = \hat{P} \times \hat{S} \times (1 - \hat{R}) \quad (5)$$

where: V_i is the composite vulnerability index of plot i (dimensionless, [0, 1]), $\hat{P}$ is the

spectral probability of disturbance from model V6-B, $\hat{S}$ is the normalized severity from the beta regression, and $\hat{R}$ is the normalized spectral recovery.

Carbon at risk per stratum was computed as:

$$C_{risk,h} = (C_{tot}/_{h}a)h \times \bar{V}_{i,h} \times Ah \quad (6)$$

where: C_risk,h is the carbon at risk of stratum h (tC), $(C\_tot/ha)_h$ the mean aboveground carbon density ($tC\ ha^{-1}$), $\bar{V}_i,h$ the within-stratum plot mean of the composite index, and A_h the area (ha).

The mean carbon density $(C\_tot/ha)_h$ was assigned uniformly to all plots within the same stratum. Concretely, the V × ρ × BEF chain (Equation 2) was applied at the stratum scale on mean stem volumes, a procedure that assumes near-homogeneous specific and structural composition within each stratum.

Hypothesis-testing procedure

The first hypothesis (H1) posited precipitation seasonality and the minimum 12-month SPEI as significant predictors of spectral disturbance probability. It was tested through the significance of V6-B coefficients (global likelihood ratio and Wald tests, 95% profile confidence intervals), and corroborated by inspecting the three warm/cool pairs at constant canopy density (S2/S1, S4/S3, S6/S5), which provided a check of spatial coherence. The second hypothesis (H2) posited higher composite vulnerability in dense stands. Its evaluation rested on ranking the within-stratum means of V_i along the open → moderate → dense gradient, paired with stratified 95% bootstrap confidence intervals (n = 5.000). Two criteria were set: monotonic ordering across the gradient, and a dense/open ratio in excess of what a biomass-only effect would predict. The test of H2 remained descriptive rather than inferential, because the limited within-stratum sample size in S3, S5, and S6 (n_h = 4–5) ruled out reliable plot-level inference.

At the annual landscape scale, correlations between the disturbed fraction and climatic descriptors (minimum 12-month SPEI, summer VPD over May–September) were computed using Pearson's coefficient over 1995–2025 (n = 31 years). The robustness of these correlations was probed by excluding 2018, which corresponded to the exceptional peak in disturbed fraction over the period, and by a Spearman cross-check on the same data. All computations and figures were produced in R 4.3.2 (R Core Team, 2023), drawing on logistf, betareg, dplyr, ggplot2, terra, sf, spsurvey, and rgee (Google Earth Engine). Bootstrap confidence intervals on V_i (n = 5.000 stratified resamples) were computed by the percentile method.

RESULTS

Structural characteristics of the stands

The 60 inventoried plots reveal a coherent structural gradient across the six strata (Table 4). Zonal mean basal area, 3.0 ± 1.7 $m^2\ ha^{-1}$ overall, climbs steadily with canopy density, from 2.1–2.3 $m^2\ ha^{-1}$ in the open strata (S1–S2) to 3.2–3.5 $m^2\ ha^{-1}$ in the moderate strata (S3–S4), and reaches 4.6–4.8 $m^2\ ha^{-1}$ in the dense strata (S5–S6). Stem density follows the same trajectory: 184–199 stems ha^{-1} in S1–S2 against 248–258 ha^{-1} in S5–S6. By contrast, mean DBH varies little (11.8–15.3 cm). Aboveground biomass spans a narrow

Table 4. Stand structure by stratum (means ± standard deviation): G, basal area; DBH, diameter at breast height; AGBD, aboveground biomass density. Per-hectare carbon stock derived from CF = 0.47

Stratum	n	G ($m^2\ ha^{-1}$)	DBH (cm)	Stems ha^{-1}	AGBD (Mg ha^{-1})	Ctot/ha (tC ha^{-1})
S1	18	2.3 ± 1.4	12.4 ± 3.1	184 ± 92	9.2 ± 4.8	4.32
S2	17	2.1 ± 1.2	11.8 ± 2.9	199 ± 107	9.1 ± 4.5	4.28
S3	4	3.5 ± 1.8	14.7 ± 2.6	207 ± 81	10.3 ± 5.1	4.84
S4	11	3.2 ± 1.6	13.9 ± 3.4	218 ± 115	10.1 ± 5.3	4.75
S5	5	4.8 ± 2.0	15.3 ± 3.8	258 ± 134	11.3 ± 5.9	5.31
S6	5	4.6 ± 1.9	14.8 ± 3.5	248 ± 128	11.0 ± 5.7	5.17
Plot mean	60	3.0 ± 1.7	13.1 ± 3.3	207 ± 106	9.8 ± 5.1	4.61

Note: The "Plot mean" row is the simple arithmetic mean across the 60 inventoried plots. The area-weighted stratum mean, underlying the total stock estimate of 122,474 tC, is AGBD = 10.0 Mg ha^{-1} and Ctot/ha = 4.69 tC ha^{-1}.

envelope, from 9.1 ± 4.5 Mg ha^{-1} in S2 to 11.3 ± 5.9 Mg ha^{-1} in S5. The plot-level mean stands at 9.8 ± 5.1 Mg ha^{-1}, while the area-weighted stratum mean, the relevant estimator for the total stock, settles at 10.0 Mg ha^{-1}.

Detection of forest disturbances

At the landscape scale, LandTrendr flagged 24,024 ha of the forest mask, or 91.9% of the area, as having gone through at least one spectral loss segment between 1995 and 2025. Plot-level prevalence reached comparable levels: 81.7% (49 of 60 plots) overall, and 80.8% (42 of 52) within the modelling subsample. Examples of LandTrendr-detected spectral trajectories for six representative plots are shown in Supplementary Figure S6. The median magnitude was moderate, with NBR variation in the 55–75 × 1.000 range, and gradual dynamics dominated the distribution (around 65% of disturbed pixels; Figure 3D). The spatial pattern (Figure 3A–B) revealed an east–west contrast, with the eastern massifs showing earlier disturbances of moderate magnitude and the western ones experiencing more recent disturbances of variable magnitude. Segment duration (Figure 3C) confirmed that gradual to chronic dynamics prevailed.

The temporal distribution showed three peaks (Figure 5A). The first, in 1995–1997 (3,700 ha), did not coincide with any 12-month SPEI drought over the area. The 2017–2019 peak culminated in 2018 at 2.4% of the area (around 625 ha yr^{-1}) and corresponded to the end of the 2016–2018 drought, with minimum $SPEI_{12}$ reaching ≈ −1.6 in 2016. The 2020–2022 peak culminated in 2021 (around 218 ha yr^{-1}) and preceded the still ongoing 2023–2024 episode, where minimum $SPEI_{12}$ fell to ≈ −2.2 in 2024. A 1- to 3-year lag was observed between SPEI minima and the temporal peaks of detected disturbances.

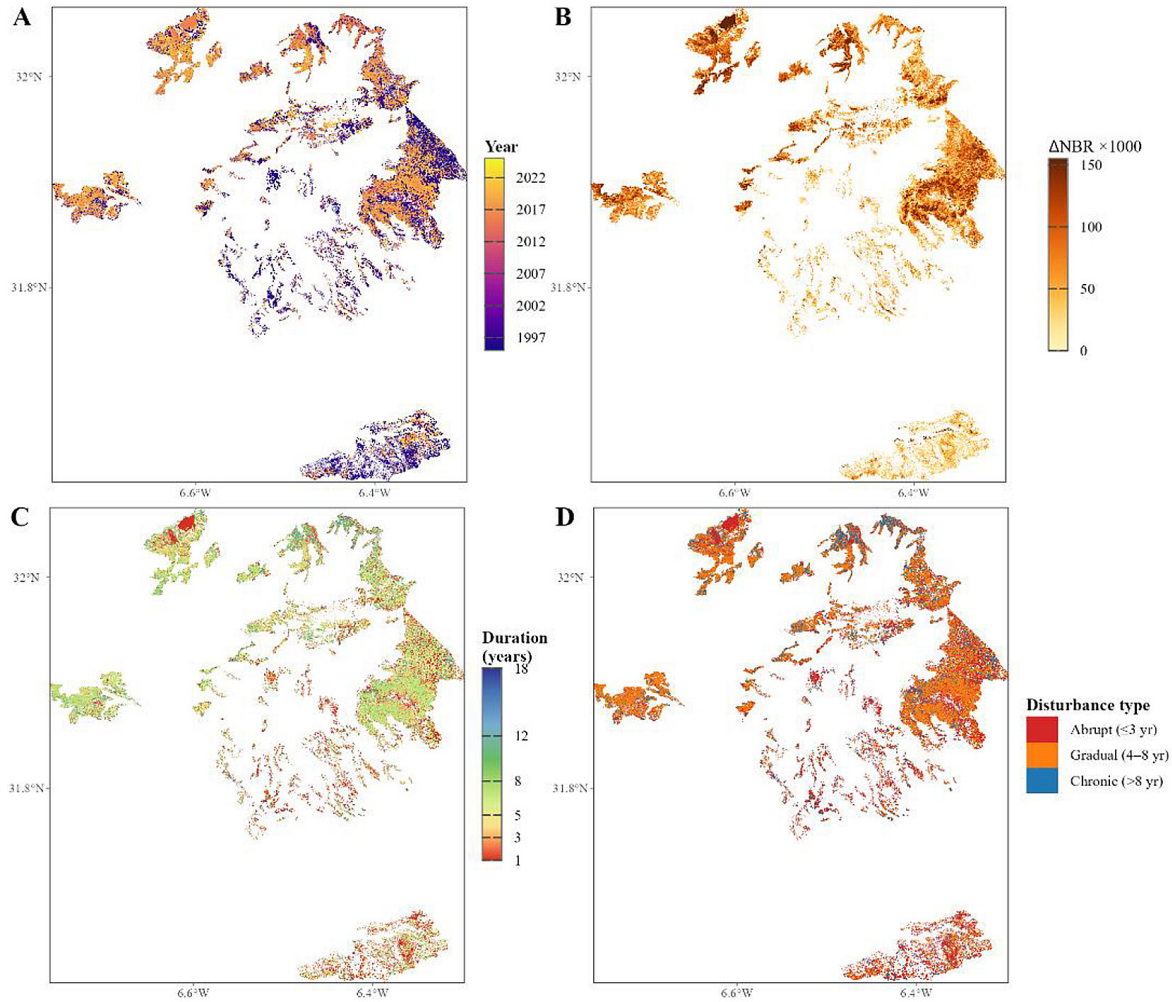

Figure 3. Spatial characterization of forest disturbances detected by LandTrendr (NBR, 1995–2025): (A) main year of disturbance; (B) magnitude (ΔNBR × 1,000, capped at the 95th percentile for readability); (C) segment duration; (D) type (abrupt, gradual, chronic)

Independent validation and climatic correlations

Validation by direct field × spectral comparison

The comparison between spectral detection and field mortality at the ≥ 15% threshold across the 60 plots (Table 5) yielded a clear pattern. Overall accuracy reached 0.800 [Wilson 95% CI: 0.682, 0.882], with field prevalence at 61.7% (37 of 60 plots). Sensitivity equalled 1.000 [0.906, 1.000]: every plot with field-confirmed mortality was also flagged by the spectral detection. Specificity reached 0.478 [0.292, 0.670], and Cohen's κ 0.531 [0.293, 0.768]. The McNemar test returned 12 false positives, 0 false negatives, and p = 0.0005. A stratum-wise decomposition of the confusion matrix is reported in Supplementary Table S2.

Annual landscape-scale correlations and climatic robustness test

The hydroclimatic context of the study area over 1995–2025 (Figure 4) combined four notable features: marked precipitation seasonality, interannual stability of reference evapotranspiration, a recurrent climatic water deficit during the warm season, and a upward trajectory of vapor pressure deficit over the past two decades.

At the annual landscape scale, neither correlation reached significance. The disturbed fraction did not correlate with the annual minimum 12-month SPEI (Pearson r = +0.11; 95% CI [−0.26, +0.46]; p = 0.55; Figure 5B), and the correlation with summer VPD over May–September fell just short of the threshold (r = −0.35; 95% CI [−0.64, +0.02]; p = 0.061; Figure 5C). Excluding the 2018 outlier (the series maximum, around 2.4% disturbed) as a robustness test left this conclusion unchanged: the SPEI correlation stayed non-significant, and the VPD correlation strengthened slightly without crossing the 0.05 threshold. The 2018 disturbed fraction (≈ 2.4%) was associated with a moderate $SPEI_{12}$ (−1.04) and a below-median summer VPD (1.31 kPa vs. 1.49 kPa over the period); the 2016–2017 values were $SPEI_{12}$ = −1.52 and −1.62, with summer VPD reaching 2.07 kPa in 2017.

Plot-level correlations between magnitude and pre-disturbance climate

At the plot level, the analysis included 44 plots that combined a detectable disturbance with fully computable pre-disturbance climatic windows from CHIRPS and ERA5-Land (Figure 6). Magnitude (ΔNBR × 1,000) correlated only weakly with the minimum 12-month SPEI preceding disturbance (R^2 = 0.03; p = 0.34; Figure 6A) and with the mean 12-month VPD (R^2 = 0.08; p = 0.066; Figure 6B). Two other descriptors crossed the significance threshold: the cumulative climatic water deficit over the 12 months before disturbance (R^2 = 0.10; p = 0.037; Figure 6C) and the mean VPD over the shorter 3-month window (R^2 = 0.10; p = 0.038; Figure 6D).

Table 5. Independent validation by direct comparison between spectral detection (prop_change > 0.5) and field mortality, defined as the proportion of stems classified as standing dead or severely declining reaching ≥ 15 % of total stems with DBH ≥ 6 cm, across the 60 inventoried plots: (a) 2 × 2 confusion matrix; (b) agreement statistics (Wilson 95% confidence intervals)

(a) Confusion matrix			
Parameter	Field: undisturbed	Field: disturbed	Total
Spectral: undisturbed	11 (TN)	0 (FN)	11
Spectral: disturbed	12 (FP)	37 (TP)	49
Total	23	37	60

(b) Agreement statistics		
Indicator	Value	95% CI
Overall accuracy	0.800	[0.682, 0.882]
Sensitivity (TP / TP+FN)	1.000	[0.906, 1.000]
Specificity (TN / TN+FP)	0.478	[0.292, 0.670]
Cohen's κ	0.531	[0.293, 0.768]
Field prevalence	0.617 (37/60)	—
McNemar test	FP = 12; FN = 0	p = 0.0005

Note: A sensitivity of 1.000 guarantees that all field mortality is captured by spectral detection. The controlled over-detection (12 FP, 0 FN) is consistent with an early spectral signature of partial dieback.

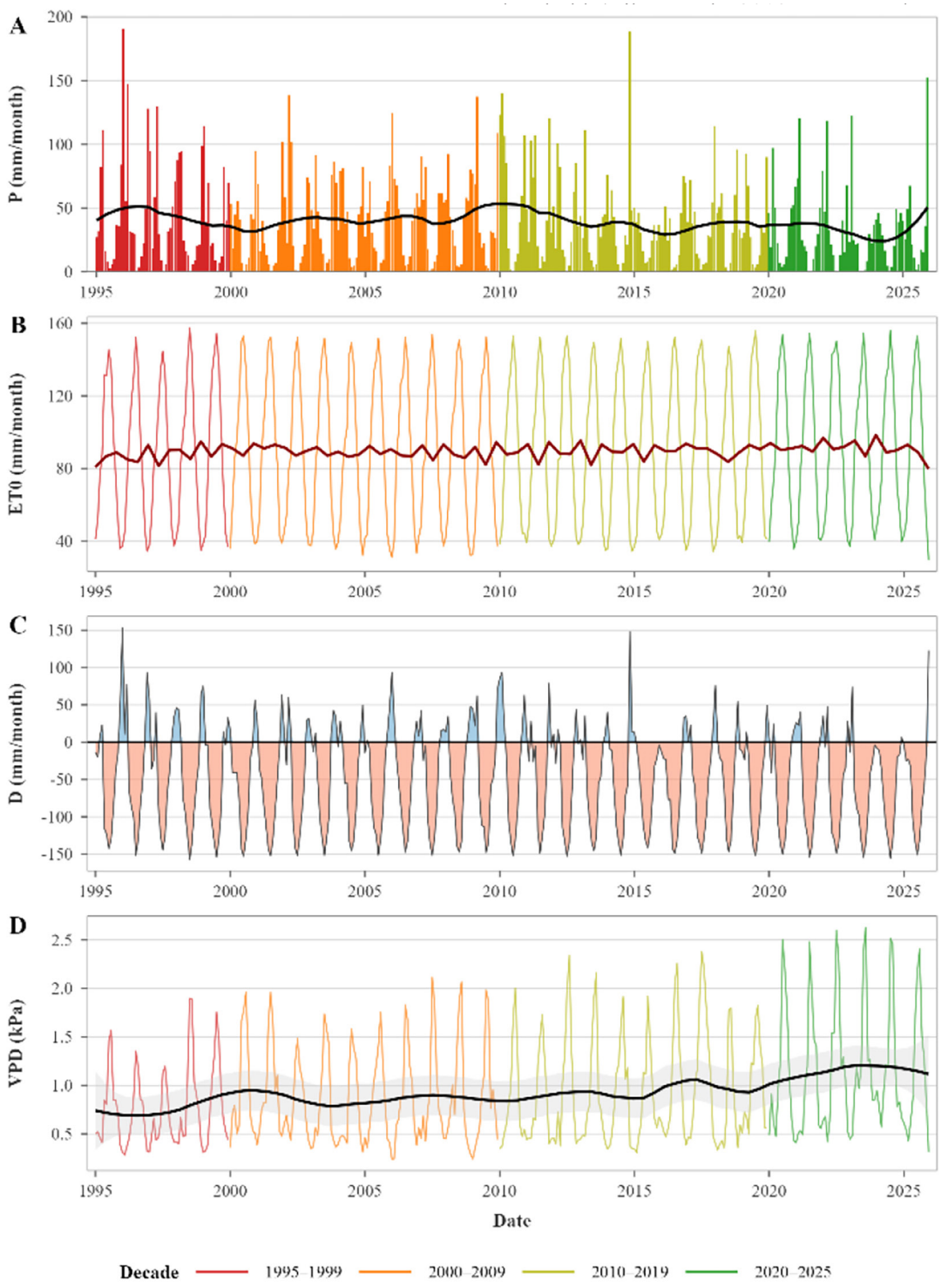

Figure 4. Hydroclimatic context of the High Atlas (study area mean), 1995–2025: (A) monthly precipitation from CHIRPS v2.0, with smoothed trend in black; (B) reference evapotranspiration computed via Penman–Monteith from ERA5-Land; (C) climatic water deficit (precipitation − evapotranspiration); (D) vapor pressure deficit

Logistic modeling of the probability of disturbance

The comparison among V2, V5, and V6-B (Table 6) placed V6-B ahead of the two alternatives. Its full AUC reached 0.827, the leave-one-out cross-validation AUC settled at 0.733, and the Riley shrinkage came out at 0.886 (Figure 7A). Within this comparison, V6-B reached the highest LOO-CV AUC (0.733), exceeding that of V5 (0.649) by 8.4 points, and its Riley shrinkage (0.886) approached the conservative 0.90

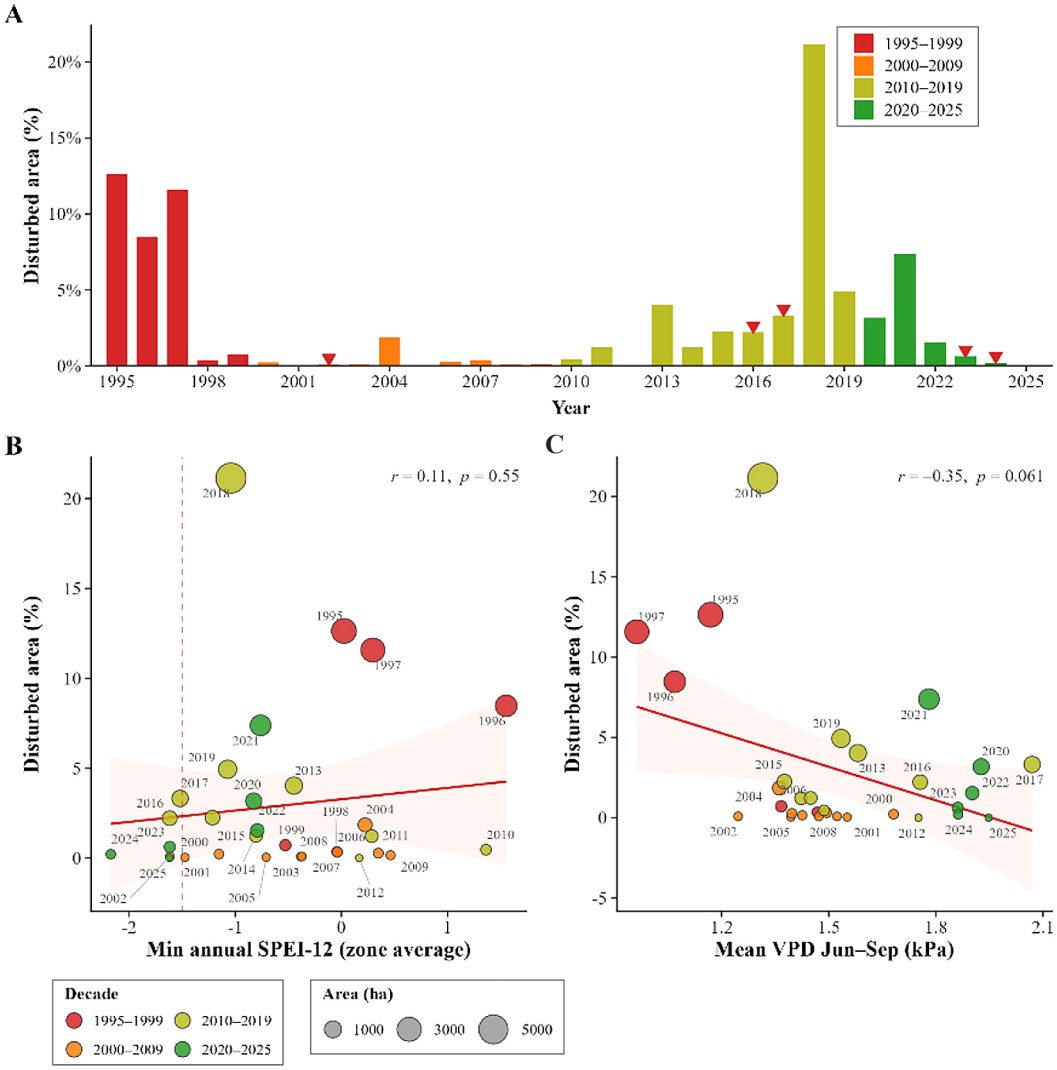

Figure 5. Forest disturbance dynamics and annual landscape-scale climatic forcing: (A) annual disturbed fraction 1995–2025 (red triangles = severe drought years, 12-month SPEI < −1.5); (B) disturbed fraction vs. annual minimum 12-month SPEI; (C) disturbed fraction vs. summer VPD (May–September)

Table 6. Comparison of the three candidate models for the probability of disturbance. Prevalence is the event rate (disturb_bin = 1) in the corresponding sample. AUC = area under the ROC curve; LOO-CV = leave-one-out cross-validation; Riley shrinkage (quality threshold ≥ 0.90 per Riley et al., 2019; van Smeden et al., 2019). Model V6-B was retained as the main model. The 52-plot subsample excludes 8 plots with incomplete pre-disturbance climatic coverage

Model	Predictors	n	Prevalence	AUC	LOO-CV	Shrinkage Riley	Role
V2	Altitude + HLI + SPEI-12 (MLE)	60	81.7%	0.654	0.645	0.984	Reference
V5	Altitude + HLI + SPEI-12 (Firth)	60	81.7%	0.753	0.649	0.862	Sensitivity
V6-B	WC_Pseas_CV + HLI + SPEI-12 (Firth)	52	80.8%	0.827	0.733	0.886	Main

(unpenalized standard maximum likelihood) was excluded outright: its LOO-CV AUC stood markedly lower at 0.645, despite a high apparent shrinkage of 0.984, a discrepancy between in-sample fit and out-of-sample performance that motivated its exclusion from the main inference.

Within V6-B, only one predictor reached statistical significance: precipitation seasonality (WC_Pseas_CV), with β = +1.184; 95% profile CI [+0.41, +2.19]; p = 0.002; global likelihood ratio test p = 0.020 (Figure 7B). Once seasonality was accounted for, neither the Heat Load Index

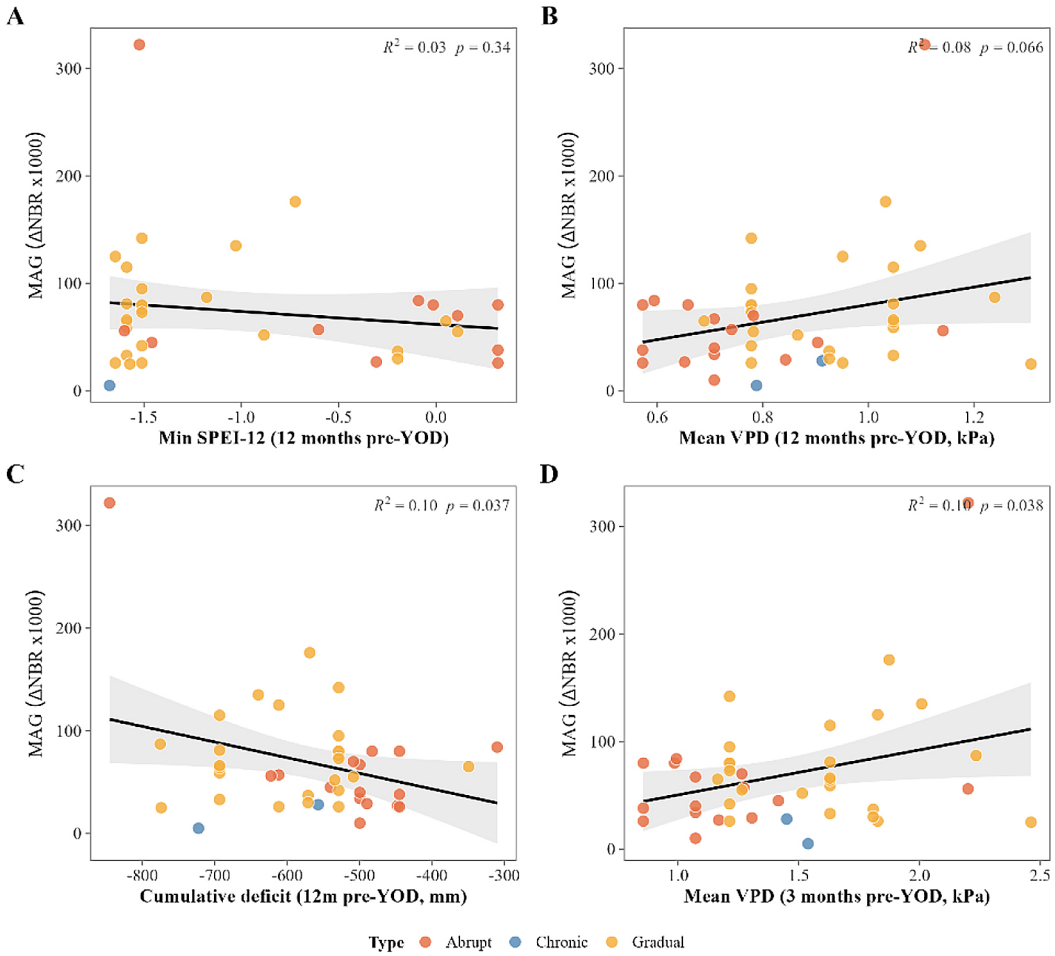

Figure 6. Plot-level correlations between magnitude and pre-disturbance climate (n = 44 disturbed plots; 3- and 12-month pre-event windows)|: (A) magnitude vs. 12-month SPEI; (B) magnitude vs. mean 12-month VPD; (C) magnitude vs. cumulative 12-month climatic water deficit; (D) magnitude vs. mean 3-month VPD. Colors indicate disturbance type

(β = −0.038) nor the minimum 12-month SPEI (β = −0.005) reached significance. The ROC curve (Figure 7A) placed V6-B (AUC = 0.827) above V5 (AUC = 0.753), with the optimal Youden threshold falling at 0.76 (sensitivity = 0.74, specificity = 0.90). The marginal effect of seasonality (Figure 7C) traced a monotonic rise from around 0.33 to around 0.95 across the observed range (47 to 65 dimensionless units).

Composite vulnerability by stratum

Across the 42 plots flagged as disturbed by LandTrendr and used for the severity model, normalized severity ranged from 0.18 to 0.69, with a mean of 0.39 ± 0.15. The beta regression on the V6-B predictors brought out a richer structure than the logistic model. Two predictors emerged as significant: precipitation seasonality (β = +0.499; SE = 0.159; p = 0.002) and the minimum 12-month SPEI (β = −0.362; SE = 0.140; p = 0.010). The Heat Load Index sat just at the edge of significance (β = −0.277; SE = 0.144; p = 0.054). The model returned a pseudo-R^2 of 0.288 and an RMSE on $\hat{S}$ of 0.202, and the residual diagnostics revealed neither marked heteroscedasticity nor systematic bias at extreme values.

Across strata, mean severity spanned a wider range than the plot-level statistics suggested. It rose from 0.294 in S1 to 0.553 in S3, with intermediate values in S5 (0.422) and S6 (0.416) (Table 7). Normalized severity stayed within the range 0.29–0.55 across the six strata.

The three components of the composite index spread out very differently across strata. Estimated probability climbed from 0.761 in S1 (open–cool) to 0.912 in S6 (dense–warm), severity from 0.294 in S1 to 0.553 in S3, and spectral recovery

Table 7. Per-stratum components of the composite vulnerability index (V_i) and of carbon at risk (Crisk)

Stratum	Area (ha)	n	$\hat{P}$	$\hat{S}$	$\hat{R}$	V_i [95% CI]	Ctot/ha	Crisk (tC)	Share of total Crisk (%)
S1	5,699	16	0.761	0.294	0.335	0.127 [0.073, 0.188]	4.32	3.120	19.5
S2	6,070	14	0.761	0.305	0.411	0.095 [0.037, 0.162]	4.28	2.470	15.5
S3	3,848	4	0.854	0.553	0.786	0.093 [0.000, 0.225]	4.84	1.730	10.8
S4	3,667	9	0.819	0.321	0.496	0.127 [0.047, 0.237]	4.75	2.210	13.8
S5	3,382	5	0.766	0.422	0.321	0.185 [0.066, 0.293]	5.31	3.320	20.8
S6	3,457	4	0.912	0.416	0.536	0.176 [0.044, 0.299]	5.17	3.140	19.6
Total	26,123	52	—	—	—	—	—	15.985	100.0

Note: $V_i = \hat{P} \times \hat{S} \times (1 - \hat{R})$ computed at the plot level and averaged by stratum; 95% CIs on V_i from non-parametric bootstrap (n = 5,000). $\hat{P}$ is from model V6-B (Firth), $\hat{S}$ from the beta regression, and $\hat{R}$ is the per-stratum mean of the [0, 1]-rescaled LandTrendr recovery score ($\hat{R}$ = 0 by convention for undisturbed plots). Row S5 is highlighted (composite hotspot). Share of total Crisk (%) gives the share of total carbon at risk attributed to each stratum (column sums to 100%); not to be confused with the within-stratum at-risk fraction. The 52-plot subsample excludes 8 plots with incomplete pre-disturbance climatic coverage

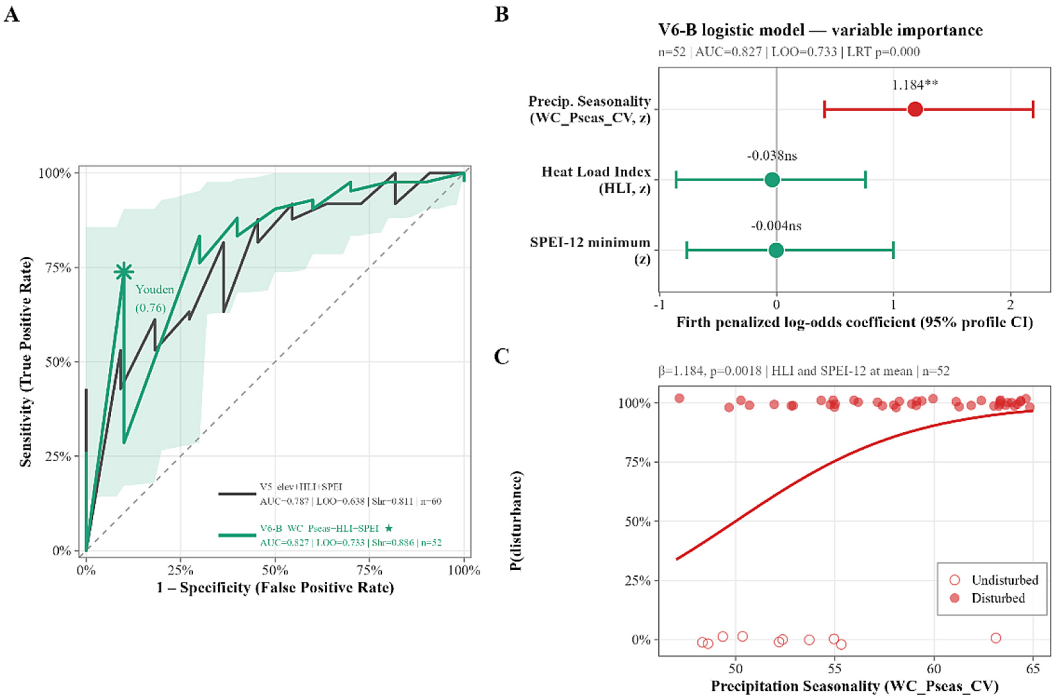

Figure 7. Penalized logistic modeling of the probability of disturbance: (A) ROC curves comparing V6-B (main model) and V5 (alternative model), with the optimal Youden threshold indicated for V6-B; (B) V6-B coefficients with 95% profile CIs; (C) marginal effect of precipitation seasonality on the probability

from 0.321 in S5 to 0.786 in S3. The two lowest recoveries belonged to S5 (0.321) and S1 (0.335), separated by less than 0.02. At the opposite end of the spectrum, S3 (0.786) combined the fastest recovery with the highest severity (0.553). The open strata S1 and S2 sat at the low-amplitude end of the regime, with the lowest probabilities (both 0.761) and severities (0.294–0.305).

The composite index peaked in S5 (Dense–cool) at 0.185 (95% bootstrap CI [0.066, 0.293]), followed by S6 at 0.176 ([0.044, 0.299]); the open and moderate strata clustered at lower values, with S1 and S4 both at 0.127 ([0.073, 0.188] and [0.047, 0.237] respectively), S2 at 0.095 ([0.037, 0.162]), and S3 at 0.093 ([0.000, 0.225]) (Figure 8A). The warm/cool pairs at constant canopy density, used as a descriptive check on thermal load, did not follow a consistent warm > cool ordering of probability. The open pair was tied (S1 = S2 = 0.761), the moderate pair ran in

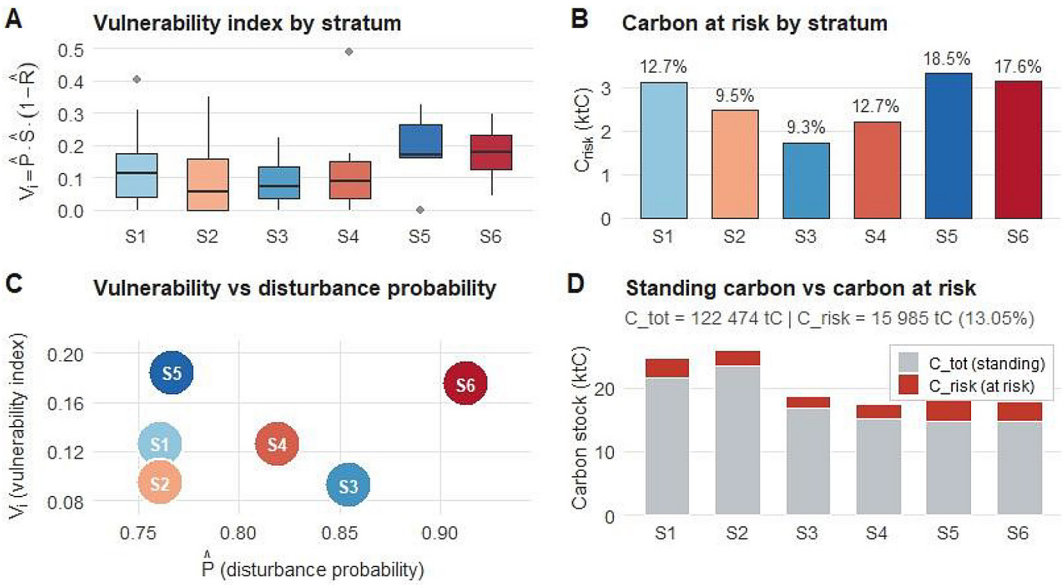

Figure 8. Composite vulnerability and carbon at risk in the High Atlas forests of Azilal (n = 52 plots): (A) vulnerability index V_i by stratum; (B) carbon at risk per stratum (bar heights in ktC), percentages above bars give the within-stratum at-risk fraction ($\bar{V}_i \times 100$), i.e. the mean composite vulnerability of the stratum — distinct from the "share of total Crisk (%)" column of Table 7, which gives the share of each stratum in the landscape total; (C) mean V_i by stratum vs. spectral probability of disturbance; (D) total aboveground carbon stock by stratum and associated at-risk fraction

the opposite direction (S3 = 0.854 above S4 = 0.819), and only the dense pair showed warm > cool (S6 = 0.912 above S5 = 0.766). Statistical diagnostics of the main V6-B model (residuals, Cook's distance, calibration plot, ROC curve) are reported in Supplementary Figure S8.

Total carbon stock and carbon at risk

Total aboveground carbon stock came to 122,474 tC, computed by per-stratum summation of weighted density multiplied by the IPCC factor of 0.47 (IPCC, 2019). Carbon at risk amounted to 15,985 tC, that is 13.05% of the total stock (stratified bootstrap 95% CI [11,654; 20,293] tC). The figure was not spread evenly across the landscape: a double hotspot in the dense strata captured most of it, with S5 (Dense–cool) holding 3.320 tC (20.8%) and S6 (Dense–warm) holding 3.140 tC (19.6%). Together, these two strata concentrated 40.4% of the zonal carbon at risk on only 26.2% of the forest area (Figure 8B). The open strata S1 and S2 carried a comparable share, 35.0% of carbon at risk (5.590 tC), but spread over a much larger 45.0% of the area. The moderate strata S3 and S4 sat in between, with 24.6% (3.940 tC) on 28.7% of the area.

DISCUSSION

To our knowledge, this study delivers the first quantitative mapping of carbon at risk for a semi-arid North African province. Three findings anchor the discussion that follows. The first concerns magnitude: carbon at risk amounted to 13.05% of total stock. The second concerns spatial concentration: a double hotspot in the dense strata (S5 and S6, 26.2% of the area) carried 40.4% of the carbon at risk. The third concerns climatic forcing: after collinearity with elevation was controlled for, precipitation seasonality emerged as the only significant spatial climatic predictor. Read together, these results point to a signature of climatic maladaptation in dense stands.

Partial validation of the first hypothesis: precipitation seasonality emerges as the dominant climatic predictor

H1 was only partially validated. Among the two climatic predictors of H1, precipitation seasonality (WC_Pseas_CV) emerged as significant in model V6-B (β = +1.184; 95% profile CI [+0.41, +2.19]; p = 0.002), with a marginal effect rising monotonically from 0.33 to 0.95 across

the observed seasonality range (Figure 7C). The minimum 12-month SPEI did not reach significance in V6-B (β = −0.005), and elevation had been previously dropped because of near-collinearity with seasonality. Precipitation seasonality jointly carries the altitudinal constraint and the Mediterranean rainfall signature, and constitutes the dominant spatial climatic predictor of disturbance probability in the study area.

An auxiliary descriptive check based on the three warm/cool pairs at constant canopy density (S2/S1, S4/S3, S6/S5) was used to inspect the spatial coherence of thermal load, in line with the procedure described in Methods (l. 160). Among the three pairs, only the dense pair showed the expected warm > cool ordering of probability (S6 = 0.912 > S5 = 0.766; Δ = +0.146); the open pair was tied (S1 = S2 = 0.761) and the moderate pair ran in the opposite direction (S3 = 0.854 > S4 = 0.819; Δ = +0.035). This descriptive check is consistent with the absence of a significant HLI effect in V6-B (β = −0.038) and reinforces the dominance of precipitation seasonality as the relevant climatic signal.

This refinement is consistent with the physiology of Mediterranean holm oaks. Limousin et al. (2010) showed that, in Quercus ilex subsp. rotundifolia, photosynthesis and stomatal conductance peak in spring, decline through summer drought, and recover with the autumn rains. Such a seasonal cycle makes interannual rainfall regularity a sharper proxy for cumulative stress than the minimum 12-month SPEI, which lumps winter and summer deficits together indistinguishably. The per-stratum spectral probabilities, ranging from 0.093 in S3 to 0.185 in S5, sat in the upper range of values reported for European forests (Forzieri et al., 2021; Senf and Seidl, 2021), placing Azilal's High Atlas among the climatically high-exposure zones.

The beta model of severity painted a different picture. Two predictors reached simultaneous significance: precipitation seasonality (β = +0.499; p = 0.002) and the minimum 12-month SPEI (β = −0.362; p = 0.010). This dissociation points to a two-step climatic control. Seasonality determines where stands become vulnerable, that is, the spatial probability of disturbance. Chronic aridity then modulates the amplitude of that disturbance once it has been triggered, that is, the conditional severity. The plot-level pre-disturbance correlations (Figure 6) reinforce this reading, since cumulative 12-month water deficit and 3-month VPD significantly modulate the observed magnitude. The between-stratum variations of normalized severity were also shaped by biomass availability: strata with higher canopy density displayed larger absolute NBR magnitudes, but the rescaling step (MAG_rel = MAG / max(MAG_stratum)) constrained the normalized values within a moderate range (0.29–0.55) and limited their direct comparability across strata of contrasting biomass.

Descriptive support for the second hypothesis: A composite vulnerability gradient from open to dense canopy

H2 is supported at the descriptive level: the within-class ordering of V_i along the canopy-density gradient places the dense strata above the open strata, with the caveat that the within-stratum sample sizes (n_h = 4–5 in S3, S5 and S6) preclude plot-level statistical inference (cf. Methods, l. 160). Mean vulnerability rose from 0.127 in S1 and 0.095 in S2 in the open strata, to 0.093 in S3 and 0.127 in S4 in the moderate strata, and reached its peak at 0.185 in S5 and 0.176 in S6 in the dense strata (Table 7). The ratio of mean vulnerability between dense (0.181) and open strata (0.111) reached a factor of 1.6, while the corresponding ratio for aboveground carbon density was 1.2 (5.24 against 4.30 tC ha^{-1}). The disproportion between the two ratios indicates that the composite concentration in the dense strata is not the simple mechanical outcome of higher available biomass, but the combined signature of probability, severity, and recovery. The bootstrap intervals (Table 7) supported this class-level ordering, while the moderate class showed a mean vulnerability (0.110) close to the open class (0.111), reflecting the non-strict monotonicity already noted.

The validation drew further support from an internal contrast within the dense strata themselves. S5 (dense–cool) carried the highest composite value (0.185), whereas a purely thermal reading would have placed S6 (dense–warm) at the top. Density class, taken as a historical proxy of the water balance at stand establishment, therefore outweighed current thermal load. This contrast is consistent with the climatic maladaptation mechanism developed in the next section, though it should be read with the caveat that within-stratum sample sizes (n_h = 4–5 in S5 and S6) preclude formal inferential testing of this pattern.

Consistency of LandTrendr detection and plot-level climatic signal

Two of the three temporal peaks (Figure 5A) coincided with the 2016–2018 and 2023–2024 droughts, with a 1- to 3-year lag in line with documented response delays (Vicente-Serrano et al., 2013; Gazol et al., 2018). The 1995–1997 peak most likely reflects temporal edge effects, as discussed under Limitations.

The 1995–1997 peak (3.700 ha) did not coincide with any 12-month SPEI drought over the area. Two non-exclusive explanations are plausible: temporal edge effects of the earliest LandTrendr segments (Kennedy et al., 2010, 2018), and a residual anthropogenic signature from late twentieth-century logging and grazing pressure described in the study-area context (l. 39, this manuscript).

At the annual landscape scale, the correlation between disturbed fraction and climatic descriptors (minimum 12-month SPEI, summer VPD) remained non-significant. This attenuation can be traced to three combined causes: the concentration of disturbances within a few pivotal years, spatial variability in lags ranging from 1 to 5 years, and dilution through landscape aggregation. The picture changed at the plot level, where the climatic signal strengthened markedly (Figure 6). Magnitude was significantly correlated with the cumulative 12-month pre-disturbance water deficit ($R^2 = 0.10$; $p = 0.037$) and with the 3-month VPD ($R^2 = 0.10$; $p = 0.038$), suggesting that disturbance magnitude is partly driven by water stress accumulated over the preceding season, which validates climatic forcing at the operationally relevant scale. The 2018 anomaly illustrates this attenuation at the year scale: an extreme disturbed fraction was associated with a moderate concurrent $SPEI_{12}$ (−1.04) and a below-median summer VPD, while the preceding 2016–2017 years had carried much more severe drought conditions ($SPEI_{12} = -1.52$ and −1.62; summer VPD = 2.07 kPa in 2017). This 1- to 2-year lag is consistent with the response delays of vegetation to drought reported at the global scale (Vicente-Serrano et al., 2013).

The coupling of sensitivity = 1.000 with specificity = 0.478 reflects an over-detection regime favoring gradual partial dieback that precedes full mortality. The McNemar pattern (12 FP, 0 FN, $p = 0.0005$) is consistent with an early spectral response to partial dieback documented for non-catastrophic disturbances (Olofsson et al., 2014; Cohen et al., 2018; Wulder et al., 2019). For management prioritisation, the point estimate of sensitivity at 1.000 (Wilson 95% CI [0.906, 1.000]) indicates a high level of early-warning capacity at the plot level, and the 12 false positives flag sites worth monitoring for early spectral signatures.

The S5/S6 double hotspot: signature of a climatic maladaptation mismatch

The S5/S6 double hotspot concentrates 40.4% of carbon at risk on 26.2% of the forested area. Within this hotspot, S5 (dense–cool) combined three unfavourable features at once. Its aboveground biomass was among the highest in the study (11.3 Mg ha^{-1}), its spectral recovery among the slowest (0.321), and its spectral probability moderate (0.766), even though its thermal load was more moderate than that of S6. This convergence signals a climatic maladaptation mismatch. The dense stands established on cool slopes likely benefited from more favourable water conditions at establishment during their developmental phase. The canopy was thereby able to densify beyond the hydraulic threshold that the current climate can sustain.

The dissociation between basal area, which differs by a factor of 2.3 between the extreme strata, and aboveground biomass, which differs by only a factor of 1.2 (Table 4), reflects the dominance of young to mid-aged cohorts originating from stump sprouts in the dense strata. In these stands, multiple stems amplify intraspecific competition for water without a matching gain in carbon storage (García-Fayos et al., 2020).

The underlying physiological mechanism is well documented for dense Mediterranean forests. Higher stand density reduces soil water availability, which triggers early stomatal closure, depresses assimilation, and produces the growth decline that typically precedes mortality (Linares and Camarero, 2012; Vilà-Cabrera et al., 2013). The meta-analysis by Sohn et al. (2016) showed that thinning systematically improves both the resistance and the resilience of residual trees during drought. At the continental scale, Bottero et al. (2017) confirmed that initial density amplifies drought-induced growth loss, especially on sites with an unfavorable water balance. At the Mediterranean regional scale, Vennetier et al. (2018) further showed that climate-induced tree

mortality varies markedly with species identity, stand composition and management history, indicating that the density-mortality link is modulated by these complementary factors.

Faced with the recent droughts of 2016–2018 and 2023–2024, S5 stands could not adjust quickly enough to keep canopy hydraulic integrity intact. Cailleret et al. (2017) showed that a precursor growth decline typically precedes mortality, with the signal sharpened in dense stands. DeSoto et al. (2020) added that post-disturbance resilience drops in trees competing for water. David et al. (2007) had earlier documented, in Q. rotundifolia, a reliance on deep water uptake that supplies up to 70% of summer transpiration, an uptake that becomes scarce in dense stands. The recovery deficit observed in S5 ($\hat{R}$ = 0.321) is thus consistent with a resilience compromised by the management history.

The climatic mismatch also fits the broader framework of Mediterranean rear-edge populations, of which the High Atlas forests stand as a paradigmatic example for Quercus rotundifolia. Carnicer et al. (2021) confirmed that resilience to warming is modulated by local topo-microclimatic conditions and by initial stand density. The composite spectral signature observed in S5 and S6 therefore aligns with a convergent body of international literature on the vulnerability of dense stands established under a past, more favorable climatic regime.

Spectral recovery and distinct slowing mechanisms between S5 and S1

The recovery deficit in S5 (0.321) signals a resilience compromised by the joint action of density and climatic maladaptation. Its numerical proximity to S1 (0.335) is, by contrast, the trace of a different dynamic, one typical of open low-biomass stands. There, recovery is slowed by recruitment limitation, low seed-tree density, restricted acorn dispersal, and scarcity of favourable microsites (Acácio and Holmgren, 2014; García-Fayos et al., 2020; Príncipe et al., 2014).

What distinguishes S5 as a composite hotspot is the conjunction of low recovery, high biomass, and high probability. S1 shares only the first of these three components, and through a different route, namely a succession blocked by recruitment limitation. The two strata diverge sharply on the other two components, with carbon density of 4.32 against 5.31 tC ha^{-1} and probability of 0.761 against 0.766. In S5, the slowing mechanism operates at two levels. The first concerns the adult cohort: trees morphologically adjusted under a past climatic regime show reduced hydraulic plasticity and remain poorly adapted to current conditions. The second concerns the juvenile cohort: young trees struggle to establish under a canopy that is still closed but already degrading, a configuration that creates transient microenvironmental conditions unfavourable to recruitment (Carnicer et al., 2021).

Consistency of biomass estimates with regional inventories and spaceborne products

The aboveground biomass density obtained by inventory, with a weighted mean of 10.0 Mg ha^{-1}, sat in the lower portion of values reported for open Mediterranean sclerophyllous forests (10–25 Mg ha^{-1}; Ruiz-Peinado et al., 2011; Montero et al., 2005; Boulmane et al., 2015; Sghaier et al., 2015). This is consistent with the aridity and elevation of the Azilal area, and stands well below the values typical of temperate or tropical sclerophyllous forests (Saatchi et al., 2011; Chave et al., 2014). Such low values correspond to carbon that is difficult to recover once lost, given the slow regeneration in semi-arid environments.

The inventory values were, by contrast, roughly five times lower than the corresponding GEDI L4A estimates (around 48 Mg ha^{-1} over the same area). This ratio is consistent with documented biases of spaceborne products in semi-arid open canopies (Rodríguez-Veiga et al., 2019). The vertical resolution of spaceborne LiDAR, combined with the scarcity of training points in arid environments, drives an upward-biased extrapolation. Two consequences follow. The first concerns the sampling design: using GEDI as a pre-inventory for Neyman allocation concentrated plots in the open strata at the expense of the dense strata, which proved to be the most critical for carbon at risk. This bias argues for a targeted inventory extension in S3, S5, and S6. The second consequence is methodological: regional carbon budgets need local inventories to be calibrated reliably, which justifies the use of locally specific allometries (Table 2).

Implications for forest management

The S5/S6 double hotspot, which carries 40.4% of carbon at risk on 26.2% of the area, deserves the highest priority for management action. Three operational axes follow from the present results.

The first axis is enhanced monitoring of the dense strata. The vulnerability mapping should be integrated directly into management plans, and inventories should be conducted every 3 to 5 years rather than every 10 years for any stand whose composite index exceeds 0.20.

The second axis is preventive thinning, targeted at the S5 stands that have crossed the operational hydraulic threshold, that is, basal area above 4 m^2 ha^{-1} together with recovery below 0.40. A 25 to 30% reduction in basal area is expected to alleviate intraspecific competition for water and to support future resilience. This recommendation is backed by Sohn et al. (2016) and D'Amato et al. (2013); the latter noted that the benefits of thinning decline with stand age, which argues for early intervention.

The third axis is assisted restoration of the open strata S1 and S2, with the focus placed on facilitating recruitment. Concrete actions include the protection of seed trees and planting in favorable microsites (Acácio and Holmgren, 2014; García-Fayos et al., 2020; Príncipe et al., 2014). Such measures are needed to preserve the long-term carbon sink function of these strata.

Study limitations and perspectives

The limitations of this work fall along six methodological dimensions.

The first concerns sampling. Sixty plots distributed over 26,123 ha limit the per-stratum precision, particularly in S3, S5, and S6, where n_h remained between 4 and 5. The Neyman allocation, anchored on GEDI L4A, concentrated 58% of plots in the open strata (35 out of 60) and only 23% in the moderate-to-dense strata combined (S3, S5, and S6 totalling 14 out of 60). These were precisely the strata that turned out to be the most critical ex post, a direct consequence of GEDI's overestimation in semi-arid open canopies. The bootstrap intervals on the composite hotspot index are accordingly wide, reaching ±60% in S5.

The second limitation is spectral. Detection rests on a single index, the NBR, and an ensemble validation across multiple indices such as NDVI and NDMI (Cohen et al., 2018) would tighten the robustness of the diagnosis. There is also a scale mismatch between the plot (0.1018 ha) and the spectral footprint (0.64 ha), which assumes a fragile homogeneity in fragmented landscapes. The temporal edge effects of LandTrendr at the start of the analysis window (1995–1997) argue for an extension back to the Landsat-4 era starting in 1982.

The third limitation is modelling. The Riley shrinkage of model V6-B ($\eta = 0.886$) remained slightly below the conservative threshold of 0.90 (Riley et al., 2019; van Smeden et al., 2019), and an independent validation cohort drawn from the Middle Atlas or another Maghreb province would be highly desirable. Diagnostics of the V5 model retained as a sensitivity analysis are reported in Supplementary Figure S9. The low n_h in S3, S5, and S6 also imposes a descriptive rather than inferential reading for these strata.

The fourth limitation lies in IPCC parameterisation. The generic biomass-to-carbon conversion factor of 0.47 was used here, rather than a value calibrated specifically for Mediterranean sclerophyllous forests. A second parameterisation issue is that assigning a uniform per-stratum carbon density through the $V \times \rho \times BEF$ chain reduces within-stratum heterogeneity to zero and may mask locally extreme combinations at the plot level.

A fifth limitation concerns the AGB estimation of *Juniperus phoenicea* and *J. oxycedrus*, for which no local allometry was available and the *J. thurifera* equation of Montero et al. (2005) was applied as a proxy. This substitution affected 3.61 % of the total aboveground biomass of the study area. Given this small fractional contribution, even a relative error of ±30 % on the proxy estimates would translate into an uncertainty of about ±1 % on the total AGB, well within the bootstrap intervals reported for carbon at risk. The substitution is therefore unlikely to alter the main conclusions of the study, but a dedicated calibration of *J. phoenicea* and *J. oxycedrus* allometries in North African conditions would remove this residual uncertainty.

A sixth limitation concerns the heterogeneity of the literature sources used to parameterize ρ and BEF across the eight inventoried species. The Monte Carlo simulation described in Materials

and Methods quantifies this uncertainty: assuming relative standard deviations of 10% on ρ and 15% on BEF, the 90% confidence interval on total AGB was [193 743; 334 333] t and on total carbon stock [91 059; 157 136] tC, around central values of 260 489 t and 122 430 tC respectively (coefficient of variation ≈ 16.5%). The relative composition was less affected: the *Juniperus* fraction of total AGB had a 90% confidence interval of [2.62%; 5.20%] around its central value of 3.65%. The main spatial conclusions of the study, expressed as relative shares (13.05% of carbon at risk, 40.4% concentration in the S5/S6 hotspot), are by construction invariant under uniform parameter perturbation and remain robust under independent species-level perturbation. A dedicated calibration of ρ and BEF for the species of the Azilal forest district would narrow this residual uncertainty. See Supplementary Figure S10 for the full Monte Carlo distribution of total AGB.

Several priority perspectives follow from these limitations. The sample should be extended to 120 to 180 plots, with the Neyman allocation recalibrated on the standard deviations actually measured in this inventory and an additional 25 to 40 plots targeted at the dense strata. An ensemble multi-index validation should be carried out. Carbon density should be computed at the plot level rather than per stratum. A local biomass-to-carbon conversion factor should be derived by dominant species.

CONCLUSIONS

This study provides the first quantitative mapping of carbon at risk at the scale of a semi-arid North African province.

The most salient operational outcome is the concentration of 40.4% of carbon at risk on 26.2% of the area, in the form of a double hotspot located in the dense strata. This result provides descriptive support for H2, with the caveat that within-stratum sample sizes (n_h = 4–5 in S3, S5 and S6) preclude plot-level statistical inference. The observed pattern—higher composite vulnerability in the dense strata—is consistent with the hypothesis that these stands were established under historically more favorable moisture regimes and now experience climatic maladaptation; this mechanism is, however, inferred from the literature on Mediterranean rear-edge forests rather than directly demonstrated by the data of the present study.

H1 was only partially validated. After controlling for near-collinearity between elevation and precipitation seasonality, the latter emerged as the only significant climatic predictor of disturbance probability in model V6-B (β = +1.184; p = 0.002), while the minimum 12-month SPEI did not reach significance (β = −0.005). The Heat Load Index, used as a topo-climatic control rather than as a predictor of H1, did not reach significance either (β = −0.038). The field validation, with perfect sensitivity and moderate specificity, reflects an over-detection regime favoring early partial dieback rather than omission of true events. The estimate of carbon at risk should therefore be read as a conservative upper bound.

The methodological approach rests on the combination of probabilistic stratification, Landsat temporal segmentation, and penalised logistic modelling, validated by a direct comparison with a field mortality inventory. The pipeline assembled here delivers a reproducible protocol for quantifying aboveground carbon at risk in semi-arid forest ecosystems.

Acknowledgements

We thank the Government of Canada for support through the New Frontiers in Research Fund [NFRFI-2023-00083], as well as the Deutsche Forschungsgemeinschaft (DFG, German Research Foundation; project number: 539520648).

REFERENCES

1. Acácio, V., Holmgren, M. (2014). Pathways for resilience in Mediterranean cork oak land use systems. *Annals of Forest Science, 71*(1), 5–13. https://doi.org/10.1007/s13595-012-0197-0
2. Allen, C. D., Breshears, D. D., McDowell, N. G. (2015). On underestimation of global vulnerability to tree mortality and forest die-off from hotter drought in the Anthropocene. *Ecosphere, 6*(8), 129. https://doi.org/10.1890/ES15-00203.1
3. Anderegg, W. R. L., Trugman, A. T., Badgley, G., Anderson, C. M., Bartuska, A., Ciais, P., Cullenward, D., Field, C. B., Freeman, J., Goetz, S. J., Hicke, J. A., Huntzinger, D., Jackson, R. B., Nickerson, J., Pacala, S., Randerson, J. T. (2020). Climate-driven risks to the climate mitigation potential of forests. *Science, 368*(6497), eaaz7005. https://doi.org/10.1126/science.aaz7005
4. Bárcenas-Pazos, G. M., Ríos-Villa, R., Aguilar-Vega, M., Díaz-Gómez, C., Velázquez-Martínez, A.,

Romero-Vargas, M. de los Á., Honorato-Salazar, J. A. (2008). Relación de las propiedades de la madera de Cupressus arizonica Greene con su densidad básica. *Revista Mexicana de Ciencias Forestales, 33*(104), 109–127.

5. Beguería, S., Vicente-Serrano, S. M., Reig, F., Latorre, B. (2014). Standardized precipitation evapotranspiration index (SPEI) revisited: parameter fitting, evapotranspiration models, tools, datasets and drought monitoring. *International Journal of Climatology, 34*(10), 3001–3023. https://doi.org/10.1002/joc.3887
6. Bottero, A., D'Amato, A. W., Palik, B. J., Bradford, J. B., Fraver, S., Battaglia, M. A., Asherin, L. A. (2017). Density-dependent vulnerability of forest ecosystems to drought. *Journal of Applied Ecology, 54*(6), 1605–1614. https://doi.org/10.1111/1365-2664.12847
7. Boulmane, M., Halim, M., Khia, A., Bensbih, H., El Hilali, M., Aafi, A., Mounir, F., Achhal, A., Cardelús, C. (2015). Estimation of forest carbon stocks in dense and reforested cedar of the Middle Atlas of Morocco. *Open Journal of Forestry, 5*(7), 661–676. https://doi.org/10.4236/ojf.2015.53023
8. Cailleret, M., Jansen, S., Robert, E. M. R., Desoto, L., Aakala, T., Antos, J. A., Beikircher, B., Bigler, C., Bugmann, H., Caccianiga, M., Čada, V., Camarero, J. J., Cherubini, P., Cochard, H., Coyea, M. R., Čufar, K., Das, A. J., Davi, H., Delzon, S., … Martínez-Vilalta, J. (2017). A synthesis of radial growth patterns preceding tree mortality. *Global Change Biology, 23*(4), 1675–1690. https://doi.org/10.1111/gcb.13535
9. Camarero, J. J., Gazol, A., Sangüesa-Barreda, G., Oliva, J., Vicente-Serrano, S. M. (2015). To die or not to die: early warnings of tree dieback in response to a severe drought. *Journal of Ecology, 103*(1), 44–57. https://doi.org/10.1111/1365-2745.12295
10. Carnicer, J., Coll, M., Ninyerola, M., Pons, X., Sánchez, G., Peñuelas, J. (2011). Widespread crown condition decline, food web disruption, and amplified tree mortality with increased climate change-type drought. *Proceedings of the National Academy of Sciences, 108*(4), 1474–1478. https://doi.org/10.1073/pnas.1010070108
11. Carnicer, J., Vives-Ingla, M., Blanquer, L., Méndez-Camps, X., Rosell-Melé, A., Lloret, F., Pinya, S., Peñuelas, J. (2021). Forest resilience to global warming is strongly modulated by local-scale topographic, microclimatic and biotic conditions. *Journal of Ecology, 109*(9), 3322–3339. https://doi.org/10.1111/1365-2745.13752
12. Chastain, R., Housman, I., Goldstein, J., Finco, M., Tenneson, K. (2019). Empirical cross sensor comparison of Sentinel-2A and 2B MSI, Landsat-8 OLI, and Landsat-7 ETM top of atmosphere spectral characteristics over the conterminous United States. *Remote Sensing of Environment, 221*, 274–285. https://doi.org/10.1016/j.rse.2018.11.012
13. Chave, J., Réjou-Méchain, M., Búrquez, A., Chidumayo, E., Colgan, M. S., Delitti, W. B. C., Duque, A., Eid, T., Fearnside, P. M., Goodman, R. C., Henry, M., Martínez-Yrízar, A., Mugasha, W. A., Muller-Landau, H. C., Mencuccini, M., Nelson, B. W., Ngomanda, A., Nogueira, E. M., Ortiz-Malavassi, E., … Vieilledent, G. (2014). Improved allometric models to estimate the aboveground biomass of tropical trees. *Global Change Biology, 20*(10), 3177–3190. https://doi.org/10.1111/gcb.12629
14. Chirici, G., McRoberts, R. E., Winter, S., Bertini, R., Brändli, U.-B., Asensio, I. A., Barbati, A., Corona, P., Marchetti, M., Travaglini, D. (2012). National forest inventory contributions to forest biodiversity monitoring. *Forest Science, 58*(3), 257–268. https://doi.org/10.5849/forsci.12-003
15. Cochran, W. G. (1977). *Sampling techniques* (3rd ed.). John Wiley & Sons.
16. Cohen, W. B., Yang, Z., Healey, S. P., Kennedy, R. E., Gorelick, N. (2018). A LandTrendr multispectral ensemble for forest disturbance detection. *Remote Sensing of Environment, 205*, 131–140. https://doi.org/10.1016/j.rse.2017.11.015
17. D'Amato, A. W., Bradford, J. B., Fraver, S., Palik, B. J. (2013). Effects of thinning on drought vulnerability and climate response in north temperate forest ecosystems. *Ecological Applications, 23*(8), 1735–1742. https://doi.org/10.1890/13-0677.1
18. David, T. S., Henriques, M. O., Kurz-Besson, C., Nunes, J., Valente, F., Vaz, M., Pereira, J. S., Siegwolf, R., Chaves, M. M., Gazarini, L. C., David, J. S. (2007). Water-use strategies in two co-occurring Mediterranean evergreen oaks: surviving the summer drought. *Tree Physiology, 27*(6), 793–803. https://doi.org/10.1093/treephys/27.6.793
19. DeSoto, L., Cailleret, M., Sterck, F., Jansen, S., Kramer, K., Robert, E. M. R., Aakala, T., Amoroso, M. M., Bigler, C., Camarero, J. J., Čufar, K., Gea-Izquierdo, G., Gillner, S., Haavik, L. J., Hereş, A.-M., Kane, J. M., Kharuk, V. I., Kitzberger, T., Klein, T., … Martínez-Vilalta, J. (2020). Low growth resilience to drought is related to future mortality risk in trees. *Nature Communications, 11*(1), 545. https://doi.org/10.1038/s41467-020-14300-5
20. Dubayah, R., Blair, J. B., Goetz, S., Fatoyinbo, L., Hansen, M., Healey, S., Hofton, M., Hurtt, G., Kellner, J., Luthcke, S., Armston, J., Tang, H., Duncanson, L., Hancock, S., Jantz, P., Marselis, S., Patterson, P. L., Qi, W., Silva, C. (2020). The Global Ecosystem Dynamics Investigation: high-resolution laser ranging of the Earth's forests and topography. *Science of Remote Sensing, 1*, 100002. https://doi.org/10.1016/j.srs.2020.100002

21. Dumelle, M., Kincaid, T. M., Olsen, A. R., Weber, M. H. (2023). Spsurvey: spatial sampling design and analysis in R. *Journal of Statistical Software, 105*(3), 1–29. https://doi.org/10.18637/jss.v105.i03
22. Duncanson, L., Kellner, J. R., Armston, J., Dubayah, R., Minor, D. M., Hancock, S., Healey, S. P., Patterson, P. L., Saarela, S., Marselis, S., Silva, C. E., Bruening, J., Goetz, S. J., Tang, H., Hofton, M., Blair, B., Luthcke, S., Fatoyinbo, L., Abernethy, K., … Zgraggen, C. (2022). Aboveground biomass density models for NASA's Global Ecosystem Dynamics Investigation (GEDI) lidar mission. *Remote Sensing of Environment, 270*, 112845. https://doi.org/10.1016/j.rse.2021.112845
23. El-Mouridi, M., Laurent, T., Famiri, A., Kabouchi, B., Alméras, T., Calchéra, G., El Abid, A., Ziani, M., Gril, J., Hakam, A. (2011). Physical characterization of argan wood (*Argania spinosa* L. Skeels). *Physical and Chemical News, 59*, 57–64.
24. Ezzahiri, M., Belghazi, B. (2000). Synthesis of some results on the natural regeneration of cork oak in the Mamora forest (Morocco). *Annales de la Recherche Forestière au Maroc, 33*, 22–32.
25. Ferrari, S., Cribari-Neto, F. (2004). Beta regression for modelling rates and proportions. *Journal of Applied Statistics, 31*(7), 799–815. https://doi.org/10.1080/0266476042000214501
26. Fick, S. E., Hijmans, R. J. (2017). WorldClim 2: new 1-km spatial resolution climate surfaces for global land areas. *International Journal of Climatology, 37*(12), 4302–4315. https://doi.org/10.1002/joc.5086
27. Firth, D. (1993). Bias reduction of maximum likelihood estimates. *Biometrika, 80*(1), 27–38. https://doi.org/10.1093/biomet/80.1.27
28. Forzieri, G., Girardello, M., Ceccherini, G., Spinoni, J., Feyen, L., Hartmann, H., Beck, P. S. A., Camps-Valls, G., Chirici, G., Mauri, A., Cescatti, A. (2021). Emergent vulnerability to climate-driven disturbances in European forests. *Nature Communications, 12*(1), 1081. https://doi.org/10.1038/s41467-021-21399-7
29. Forzieri, G., Dakos, V., McDowell, N. G., Ramdane, A., Cescatti, A. (2022). Emerging signals of declining forest resilience under climate change. *Nature, 608*(7923), 534–539. https://doi.org/10.1038/s41586-022-04959-9
30. Frazier, R. J., Coops, N. C., Wulder, M. A., Hermosilla, T., White, J. C. (2018). Analyzing spatial and temporal variability in short-term rates of post-fire vegetation return from Landsat time series. *Remote Sensing of Environment, 205*, 32–45. https://doi.org/10.1016/j.rse.2017.11.007
31. Funk, C., Peterson, P., Landsfeld, M., Pedreros, D., Verdin, J., Shukla, S., Husak, G., Rowland, J., Harrison, L., Hoell, A., Michaelsen, J. (2015). The climate hazards infrared precipitation with stations—a new environmental record for monitoring extremes. *Scientific Data, 2*, 150066. https://doi.org/10.1038/sdata.2015.66
32. García-Fayos, P., Monleon, V. J., Espigares, T., Nicolau, J. M., Bochet, E. (2020). Increasing aridity threatens the sexual regeneration of *Quercus ilex* (holm oak) in Mediterranean ecosystems. *PLOS ONE, 15*(10), e0239755. https://doi.org/10.1371/journal.pone.0239755
33. Gazol, A., Camarero, J. J., Vicente-Serrano, S. M., Sánchez-Salguero, R., Gutiérrez, E., de Luis, M., Sangüesa-Barreda, G., Novak, K., Rozas, V., Tíscar, P. A., Linares, J. C., Martín-Hernández, N., Martínez del Castillo, E., Ribas, M., García-González, I., Silla, F., Camisón, A., Génova, M., Olano, J. M., … Galván, J. D. (2018). Forest resilience to drought varies across biomes. *Global Change Biology, 24*(5), 2143–2158. https://doi.org/10.1111/gcb.14082
34. Gorelick, N., Hancher, M., Dixon, M., Ilyushchenko, S., Thau, D., Moore, R. (2017). Google Earth Engine: planetary-scale geospatial analysis for everyone. *Remote Sensing of Environment, 202*, 18–27. https://doi.org/10.1016/j.rse.2017.06.031
35. Hair, J. F., Black, W. C., Babin, B. J., Anderson, R. E. (2014). *Multivariate Data Analysis* (7th ed.). Pearson Education.
36. Hannah, L., Flint, L., Syphard, A. D., Moritz, M. A., Buckley, L. B., McCullough, I. M. (2014). Fine-grain modeling of species' response to climate change: holdouts, stepping-stones, and microrefugia. *Trends in Ecology & Evolution, 29*(7), 390–397. https://doi.org/10.1016/j.tree.2014.04.006
37. Heinze, G., Schemper, M. (2002). A solution to the problem of separation in logistic regression. *Statistics in Medicine, 21*(16), 2409–2419. https://doi.org/10.1002/sim.1047
38. Henry, M., Picard, N., Trotta, C., Manlay, R., Valentini, R., Bernoux, M., Saint-André, L. (2011). Estimating tree biomass of sub-Saharan African forests: a review of available allometric equations. *Silva Fennica, 45*(3B), 477–569. https://doi.org/10.14214/sf.38
39. IPCC. (2019). *2019 refinement to the 2006 IPCC guidelines for national greenhouse gas inventories*. Volume 4: Agriculture, forestry and other land use. IPCC.
40. IPCC. (2022). *Climate change 2022: impacts, adaptation and vulnerability*. Contribution of Working Group II to the Sixth Assessment Report of the Intergovernmental Panel on Climate Change (H.-O. Pörtner, D. C. Roberts, M. Tignor, E. S. Poloczanska, K. Mintenbeck, A. Alegría, M. Craig, S. Langsdorf, S. Löschke, V. Möller, A. Okem, & B. Rama, Eds.). Cambridge University Press. https://doi.org/10.1017/9781009325844
41. Kennedy, R. E., Yang, Z., Cohen, W. B. (2010). Detecting trends in forest disturbance and recovery using yearly Landsat time series: 1. LandTrendr

— temporal segmentation algorithms. *Remote Sensing of Environment, 114*(12), 2897–2910. https://doi.org/10.1016/j.rse.2010.07.008

42. Kennedy, R. E., Yang, Z., Gorelick, N., Braaten, J., Cavalcante, L., Cohen, W. B., Healey, S. (2018). Implementation of the LandTrendr algorithm on Google Earth Engine. *Remote Sensing, 10*(5), 691. https://doi.org/10.3390/rs10050691
43. Limousin, J.-M., Misson, L., Lavoir, A.-V., Martin, N. K., Rambal, S. (2010). Do photosynthetic limitations of evergreen Quercus ilex leaves change with long-term increased drought severity? *Plant, Cell & Environment, 33*(5), 863–875. https://doi.org/10.1111/j.1365-3040.2009.02112.x
44. Linares, J. C., Camarero, J. J. (2012). From pattern to process: linking intrinsic water-use efficiency to drought-induced forest decline. *Global Change Biology, 18*(3), 1000–1015. https://doi.org/10.1111/j.1365-2486.2011.02566.x
45. McCune, B., Keon, D. (2002). Equations for potential annual direct incident radiation and heat load. *Journal of Vegetation Science, 13*(4), 603–606. https://doi.org/10.1111/j.1654-1103.2002.tb02087.x
46. Montero, G., Ruiz-Peinado, R., Muñoz, M. (2005). Producción de biomasa y fijación de CO_2 por los bosques españoles. *Monografías INIA: Serie Forestal, 13*. Ministerio de Educación y Ciencia.
47. Muñoz-Sabater, J., Dutra, E., Agustí-Panareda, A., Albergel, C., Arduini, G., Balsamo, G., Boussetta, S., Choulga, M., Harrigan, S., Hersbach, H., Martens, B., Miralles, D. G., Piles, M., Rodríguez-Fernández, N. J., Zsoter, E., Buontempo, C., Thépaut, J.-N. (2021). ERA5-Land: a state-of-the-art global reanalysis dataset for land applications. *Earth System Science Data, 13*(9), 4349–4383. https://doi.org/10.5194/essd-13-4349-2021
48. Olofsson, P., Foody, G. M., Herold, M., Stehman, S. V., Woodcock, C. E., Wulder, M. A. (2014). Good practices for estimating area and assessing accuracy of land change. *Remote Sensing of Environment, 148*, 42–57. https://doi.org/10.1016/j.rse.2014.02.015
49. Pan, Y., Birdsey, R. A., Fang, J., Houghton, R., Kauppi, P. E., Kurz, W. A., Phillips, O. L., Shvidenko, A., Lewis, S. L., Canadell, J. G., Ciais, P., Jackson, R. B., Pacala, S. W., McGuire, A. D., Piao, S., Rautiainen, A., Sitch, S., Hayes, D. (2011). A large and persistent carbon sink in the world's forests. *Science, 333*(6045), 988–993. https://doi.org/10.1126/science.1201609
50. Pasquarella, V. J., Arévalo, P., Bratley, K. H., Bullock, E. L., Gorelick, N., Zhu, Z., Kennedy, R. E. (2022). Demystifying LandTrendr and CCDC temporal segmentation. *International Journal of Applied Earth Observation and Geoinformation, 110*, 102806. https://doi.org/10.1016/j.jag.2022.102806
51. Príncipe, A., Nunes, A., Pinho, P., Do Rosário, L., Correia, O., Branquinho, C. (2014). Modeling the long-term natural regeneration potential of woodlands in semi-arid regions to guide restoration efforts. *European Journal of Forest Research, 133*(5), 757–767. https://doi.org/10.1007/s10342-014-0787-5
52. R Core Team. (2023). R: a language and environment for statistical computing (Version 4.3.2) [Software]. R Foundation for Statistical Computing. https://www.R-project.org/
53. Riley, R. D., Snell, K. I. E., Ensor, J., Burke, D. L., Harrell Jr., F. E., Moons, K. G. M., Collins, G. S. (2019). Minimum sample size for developing a multivariable prediction model: PART II — binary and time-to-event outcomes. *Statistics in Medicine, 38*(7), 1276–1296. https://doi.org/10.1002/sim.7992
54. Rodríguez-Veiga, P., Quegan, S., Carreiras, J., Persson, H. J., Fransson, J. E. S., Hoscilo, A., Ziółkowski, D., Stereńczak, K., Lohberger, S., Stängel, M., Berninger, A., Siegert, F., Avitabile, V., Herold, M., Mermoz, S., Bouvet, A., Le Toan, T., Carvalhais, N., Santoro, M., … Balzter, H. (2019). Forest biomass retrieval approaches from earth observation in different biomes. *International Journal of Applied Earth Observation and Geoinformation, 77*, 53–68. https://doi.org/10.1016/j.jag.2018.12.008
55. Ruiz-Peinado, R., del Río, M., Montero, G. (2011). New models for estimating the carbon sink capacity of Spanish softwood species. *Forest Systems, 20*(1), 176–188. https://doi.org/10.5424/fs/2011201-11643
56. Ruiz-Peinado, R., Montero, G., del Río, M. (2012). Biomass models to estimate carbon stocks for hardwood tree species. *Forest Systems, 21*(1), 42–52. https://doi.org/10.5424/fs/2112211-02193
57. Saatchi, S. S., Harris, N. L., Brown, S., Lefsky, M., Mitchard, E. T. A., Salas, W., Zutta, B. R., Buermann, W., Lewis, S. L., Hagen, S., Petrova, S., White, L., Silman, M., Morel, A. (2011). Benchmark map of forest carbon stocks in tropical regions across three continents. *Proceedings of the National Academy of Sciences, 108*(24), 9899–9904. https://doi.org/10.1073/pnas.1019576108
58. Senf, C., Seidl, R. (2021). Mapping the forest disturbance regimes of Europe. *Nature Sustainability, 4*(1), 63–70. https://doi.org/10.1038/s41893-020-00609-y
59. Sghaier, T., Sánchez-González, M., Garchi, S., Ammari, Y., Cañellas, I., Calama, R. (2015). Developing a stand-based growth and yield model for Thuya (Tetraclinis articulata (Vahl) Mast) in Tunisia. *iForest – Biogeosciences and Forestry, 9*(1), 79–88. https://doi.org/10.3832/ifor1389-008
60. Shaiek, O., Loustau, D., Trichet, P., Meredieu, C., Bachtobji, B., Garchi, S., El Aouni, M. H. (2011). Generalized biomass equations for the main aboveground biomass components of maritime pine

across contrasting environments. *Annals of Forest Science, 68*(3), 443–452. https://doi.org/10.1007/s13595-011-0044-8

61. Sohn, J. A., Saha, S., Bauhus, J. (2016). Potential of forest thinning to mitigate drought stress: a meta-analysis. *Forest Ecology and Management, 380*, 261–273. https://doi.org/10.1016/j.foreco.2016.07.046
62. Stevens, D. L., Olsen, A. R. (2004). Spatially balanced sampling of natural resources. *Journal of the American Statistical Association, 99*(465), 262–278. https://doi.org/10.1198/016214504000000250
63. Tramblay, Y., Koutroulis, A., Samaniego, L., Vicente-Serrano, S. M., Volaire, F., Boone, A., Le Page, M., Llasat, M. C., Albergel, C., Burak, S., Cailleret, M., Kalin, K. C., Davi, H., Dupuy, J.-L., Greve, P., Grillakis, M., Hanich, L., Jarlan, L., Martin-StPaul, N., … Polcher, J. (2020). Challenges for drought assessment in the Mediterranean region under future climate scenarios. *Earth-Science Reviews, 210*, 103348. https://doi.org/10.1016/j.earscirev.2020.103348
64. Vallet, P., Dhôte, J.-F., Le Moguédec, G., Ravart, M., Pignard, G. (2006). Development of total aboveground volume equations for seven important forest tree species in France. *Forest Ecology and Management, 229*(1–3), 98–110. https://doi.org/10.1016/j.foreco.2006.03.013
65. van Smeden, M., Moons, K. G. M., de Groot, J. A. H., Collins, G. S., Altman, D. G., Eijkemans, M. J. C., Reitsma, J. B. (2019). Sample size for binary logistic prediction models: beyond events per variable criteria. *Statistical Methods in Medical Research, 28*(8), 2455–2474. https://doi.org/10.1177/0962280218784726
66. Vennetier, M., Chandioux, O., Ripert, C., Estève, R., Crouzet, B., Gilg, O., Prévosto, B., Cailleret, M., Martin-StPaul, N., Davi, H., Mouillot, F. (2018). Climate change impact on tree mortality differs according to species, stand composition and management in Mediterranean forests. In: F. Bravo-Oviedo, V. LeMay, R. Jandl, & K. von Gadow (Eds.), Managing forest ecosystems: the challenge of climate change (Vol. 34, pp. 319–338). Springer.
67. Vicente-Serrano, S. M., Beguería, S., López-Moreno, J. I. (2010). A multiscalar drought index sensitive to global warming: the standardized precipitation evapotranspiration index. *Journal of Climate, 23*(7), 1696–1718. https://doi.org/10.1175/2009JCLI2909.1
68. Vicente-Serrano, S. M., Gouveia, C., Camarero, J. J., Beguería, S., Trigo, R., López-Moreno, J. I., Azorín-Molina, C., Pasho, E., Lorenzo-Lacruz, J., Revuelto, J., Morán-Tejeda, E., Sanchez-Lorenzo, A. (2013). Response of vegetation to drought time-scales across global land biomes. *Proceedings of the National Academy of Sciences, 110*(1), 52–57. https://doi.org/10.1073/pnas.1207068110
69. Vignote, S., Molinero, I., Gerard, J., Diez, M. R. (2006). Estudio de la influencia de la aplicación de calor por la cara izquierda de un tronco de Cupressus arizonica para usar en aserrío. *Forest Systems, 15*(1), 71–79.
70. Vilà-Cabrera, A., Martínez-Vilalta, J., Galiano, L., Retana, J. (2013). Patterns of forest decline and regeneration across Scots pine populations. *Ecosystems, 16*(2), 323–335. https://doi.org/10.1007/s10021-012-9615-2
71. Wulder, M. A., Loveland, T. R., Roy, D. P., Crawford, C. J., Masek, J. G., Woodcock, C. E., Allen, R. G., Anderson, M. C., Belward, A. S., Cohen, W. B., Dwyer, J., Erb, A., Gao, F., Griffiths, P., Helder, D., Hermosilla, T., Hipple, J. D., Hostert, P., Hughes, M. J., … Zhu, Z. (2019). Current status of Landsat program, science, and applications. *Remote Sensing of Environment, 225*, 127–147. https://doi.org/10.1016/j.rse.2019.02.015
72. Zhu, Z., Woodcock, C. E. (2014). Continuous change detection and classification of land cover using all available Landsat data. *Remote Sensing of Environment, 144*, 152–171. https://doi.org/10.1016/j.rse.2014.01.011